

# Transition from the Infalling Envelope to the Keplerian Disk around L1551 IRS 5

Ti-Lin Chou<sup>1,2</sup>, Shigehisa Takakuwa<sup>2</sup>, Hsi-Wei Yen<sup>2</sup>, Nagayoshi Ohashi<sup>2,3</sup>, & Paul T. P. Ho<sup>2,4</sup>

## ABSTRACT

We present combined SubMillimeter Array (SMA) + Atacama Submillimeter Telescope Experiment (ASTE) images of the Class I protobinary L1551 IRS 5 in the CS ( $J = 7-6$ ) line, the submillimeter images of L1551 IRS 5 with the most complete spatial sampling ever achieved ( $0''.9 - 36''$ ). The SMA image of L1551 IRS 5 in the 343 GHz dust-continuum emission is also presented, which shows an elongated feature along the northwest to southeast direction ( $\sim 160 \text{ AU} \times 80 \text{ AU}$ ), perpendicular to the associated radio jets. The combined SMA+ASTE images show that the high-velocity ( $\gtrsim 1.5 \text{ km s}^{-1}$ ) CS emission traces the structure of the dust component and shows a velocity gradient along the major axis, which is reproduced by a geometrically-thin Keplerian-disk model with a central stellar mass of  $\sim 0.5 M_{\odot}$ . The low-velocity ( $\lesssim 1.3 \text{ km s}^{-1}$ ) CS emission shows an extended ( $\sim 1000 \text{ AU}$ ) feature that exhibits slight south (blueshifted) to north (redshifted) emission offsets, which is modeled with a rotating and infalling envelope with a conserved angular momentum. The rotational motion of the envelope connects smoothly to the inner Keplerian rotation at a radius of  $\sim 64 \text{ AU}$ . The infalling velocity of the envelope is  $\sim$ three times lower than the free-fall velocity toward the central stellar mass of  $0.5 M_{\odot}$ . These results demonstrate transition from the infalling envelope to the Keplerian disk, consistent with the latest theoretical studies of disk formation. We suggest that sizable ( $r \sim 50-200 \text{ AU}$ ) Keplerian disks are already formed when the protostars are still deeply embedded in the envelopes.

*Subject headings:* ISM: molecules — ISM: individual (L1551 IRS 5) — stars: formation

## 1. Introduction

Keplerian disks are ubiquitous around T-Tauri (Class II) sources (*e.g.*, Simon et al. 2000), and are considered to be the nurseries of planetary systems. Around younger protostellar

---

<sup>1</sup>Department of Physics, National Taiwan University, No. 1, Sec. 4, Roosevelt Rd., Taipei 106, Taiwan; tl-chou@asiaa.sinica.edu.tw

<sup>2</sup>Academia Sinica Institute of Astronomy and Astrophysics, P. O. Box 23-141, Taipei 10617, Taiwan

<sup>3</sup>Subaru Telescope, National Astronomical Observatory of Japan, 650 North A'ohoku Place, Hilo, HI 96720, USA

<sup>4</sup>Harvard-Smithsonian Center for Astrophysics, 60 Garden Street, Cambridge, MA 02138, USA

(Class 0–I) sources there are  $\sim 2000$ – $10000$  AU scale protostellar envelopes that often show rotating and infalling gas motions (Ohashi et al. 1996; Ohashi et al. 1997; Momose et al. 1998; Takakuwa et al. 2003; Takakuwa et al. 2007). Recent high-resolution interferometric observations in (sub)millimeter molecular lines have found Keplerian disks around protostellar sources (Brinch et al. 2007; Lommen et al. 2008; Jørgensen et al. 2009; Takakuwa et al. 2012; Tobin et al. 2012; Hara et al. 2013; Murillo et al. 2013; Takakuwa et al. 2013; Yen et al. 2013; Yen et al. 2014; Harsono et al. 2014; Lee et al. 2014; Takakuwa et al. 2014; Ohashi et al. 2014). The masses ( $\sim 0.01$ – $0.03 M_{\odot}$ ) and radii ( $\sim 80$ – $300$  AU) of these Keplerian disks around protostars are comparable to those of circumstellar disks around T-Tauri stars (Guilloteau & Dutrey 1998; Guilloteau et al. 1999; Andrews & Williams 2005; Andrews & Williams 2007; Schaefer et al. 2009). These results show that formation of Keplerian disks proceeds in the innermost parts of the infalling envelopes.

It remains controversial as to how Keplerian disks form out of the infalling envelopes around protostars. Mellon & Li (2008; 2009), and Li et al. (2011) have performed magnetohydrodynamic (MHD) simulations of self-similar, collapsing envelopes to investigate the formation of Keplerian disks. They found that, for typical magnetic field strengths in interstellar clouds, magnetic braking is so efficient that rotationally-supported disks cannot form. On the other hand, recent theoretical simulations by Machida & Hosokawa (2013) and Machida et al. (2014) successfully produced rotationally supported disks, with their masses comparable to the observed results. Their argument is that the Ohmic dissipation and the dispersal of the surrounding infalling envelope that anchors the magnetic field significantly reduce the effect of the magnetic field on the disk formation.

To put stringent observational constraints on the theories of disk formation, direct imaging of the transition from infalling envelopes to Keplerian disks, and studies of evolutions of Keplerian disks embedded in infalling envelopes, are crucial. Takakuwa et al. (2013) have found infalling gas outside of the Keplerian disk around L1551 NE, a Class I protobinary located  $\sim 2.5$  north-east of L1551 IRS 5, and revealed that the angular momentum of the infalling gas is much smaller than that of the Keplerian disk. Furthermore, the infalling velocity onto the central Keplerian disk is much smaller than the free-fall velocity toward the central stellar mass of  $0.8 M_{\odot}$  as derived from the Keplerian rotation. These results suggest a reduced infalling velocity and possible magnetic braking which decreases the rotational angular momentum of the infalling material. A slower infalling velocity than the free-fall velocity has also been identified in the envelope surrounding a Keplerian disk around a Class 0/I protostar L1527 IRS (Ohashi et al. 2014). On the other hand, Yen et al. (2014) found parabolic free-falling flows where the rotational angular momentum is conserved enroute to the central Keplerian disk around L1489 IRS. These observational reports are so far the only examples of the transition from the infalling envelopes to the Keplerian disks. Hence, a general picture of the transition, and the evolutionary sequence of Keplerian disks embedded in infalling envelopes, are not yet established.

In order to further study the formation mechanism of Keplerian disks, we have performed Sub-

Millimeter Array (SMA)<sup>1</sup> observations of L1551 IRS 5, one of the best-studied Class I protostars, in the submillimeter continuum and CS ( $J=7-6$ ) emission. The SMA CS ( $7-6$ ) data were combined with the single-dish mapping data of CS ( $7-6$ ) from the Atacama Submillimeter Telescope Experiment (ASTE)<sup>2</sup> (Takakuwa & Kamazaki 2011). L1551 IRS 5 is a protostellar binary system with a projected separation of  $\sim 0.3''$  (Looney et al. 1997; Rodríguez et al. 1998; Lim & Takakuwa 2006), located in Taurus at a distance of 140 pc (Kenyon et al. 1994). The two binary sources, located to the north and south, both drive active radio jets along the northeast to southwest direction (Rodríguez et al. 2003). Previous interferometric observations of L1551 IRS 5 in millimeter molecular lines have found a  $\sim 2500$  AU-scale rotating and infalling envelope surrounding the protobinary (Ohashi et al. 1996; Saito et al. 1996; Momose et al. 1998). The rotational motion in the envelope shows a radial dependence of  $v_{rot} \propto r^{-1}$  at a radii of  $\sim 300 - 1000$  AU, which is consistent with the conserved angular momentum. The infall velocity over those radii is also consistent with free-fall toward a central stellar mass of  $0.1 M_{\odot}$ . For radii at  $< 300$  AU, higher-velocity ( $\gtrsim 0.7$  km s $^{-1}$ ) features are present, which indicates that the central mass should be as high as  $0.5 M_{\odot}$  (Momose et al. 1998). Our previous SMA observations of L1551 IRS 5 in CS ( $7-6$ ) found rotation-dominant gas motion in the inner  $\sim 400$  AU scale of the protostellar envelope, suggesting the presence of a Keplerian disk (Takakuwa et al. 2004). However, the lower angular resolution in the SMA early science study ( $\sim 3''.2 \times 2''.0$ ) prevented us from unambiguously identifying the Keplerian disk. Our new SMA observations at a subarcsecond resolution, when combined with the single-dish ASTE data, enable us to investigate the spatial and kinematical structures with the most complete spatial sampling ever achieved ( $\sim 0''.9 - 36''$ ). With these data, we have successfully identified the inner Keplerian disk and the transition from the outer infalling envelope.

In the following, we describe our SMA observations (Section 2), our continuum and molecular-line results (Section 3), and the analysis to identify the Keplerian disk and the infalling envelope (Section 4). In the last section (Section 5), we will compare the properties of the Keplerian disk and envelope around L1551 IRS 5 to those of the theoretical predictions and around the other protostars. Then we discuss the formation and the evolutionary mechanism of Keplerian disks embedded in infalling envelopes.

## 2. SMA Observations and Combining with the ASTE Data

We observed L1551 IRS 5 with the SMA in its subcompact configuration on 2009 September 21, and in its extended configuration on 2012 December 23 and 2013 January 4. Details of the SMA are

---

<sup>1</sup>The SMA is a joint project between the Smithsonian Astrophysical Observatory and the Academia Sinica Institute of Astronomy and Astrophysics and is funded by the Smithsonian Institution and the Academia Sinica.

<sup>2</sup>The ASTE project is driven by Nobeyama Radio Observatory (NRO), a branch of National Astronomical Observatory of Japan (NAOJ), in collaboration with University of Chile, and Japanese institutes including University of Tokyo, Nagoya University, Osaka Prefecture University, Ibaraki University, and Hokkaido University.

described by Ho et al. (2004). In the observation with the subcompact configuration, CS ( $J=7-6$ ; 342.882857 GHz),  $\text{HC}^{15}\text{N}$  ( $J=4-3$ ; 344.200109 GHz), SO ( $J_N=8_8-7_7$ ; 344.310612 GHz), and HCN ( $J=4-3$ ; 354.505473 GHz) lines, and continuum emission at both the upper and lower sidebands with the LO frequency of 348.754 GHz and the IF range of 4–6 GHz were measured simultaneously. In the observations with the extended configuration, CS ( $J=7-6$ ),  $\text{C}^{18}\text{O}$  ( $J=3-2$ ; 329.3305453 GHz),  $^{13}\text{CO}$  ( $J=3-2$ ; 330.587965 GHz), and SO ( $J_N=8_8-7_7$ ) lines, and continuum emission at both the upper and lower sidebands with the LO frequency of 336.902 GHz and the IF range of 4–8 GHz were measured simultaneously. The SMA correlator consists of a bank of the spectral windows (“chunks”) with a bandwidth of 82 MHz, and there are totally 22 and 42 chunks at each sideband in the observations with the subcompact and extended configurations, respectively. The chunk assigned to the CS line had a spectral resolution of 203.125 kHz, corresponding to a velocity resolution of  $0.178 \text{ km s}^{-1}$ . The raw visibility data were calibrated and flagged with MIR, which is an IDL-based data reduction package (Scoville et al. 1993). All the chunks at both sidebands except for those assigned for the strong molecular lines were combined to make a single continuum channel, providing the total continuum bandwidth 3.444 GHz in the subcompact observation and 6.560 GHz in the extended observations. Both the continuum channels taken in the subcompact and extended observations were co-added, and the continuum image was generated with uniform weighting of the measured visibilities. In the present paper, we will focus on the results of the continuum emission (hereafter 343 GHz continuum emission) and the CS (7–6) line. The CS line was observed with the SMA subcompact and extended configurations, and with ASTE (see below). The SMA  $^{13}\text{CO}$ ,  $\text{C}^{18}\text{O}$ , and SO data exhibit an emission component centered on the protobinary, with a northwest (redshifted) to southeast (blueshifted) velocity gradient, similar to that of the CS data. The velocity gradient in the HCN line is not clear because of the hyperfine blending, and the  $\text{HC}^{15}\text{N}$  line is too weak to identify the velocity structure.

We combined the SMA CS (7–6) data with the ASTE single-dish CS (7–6) data (Takakuwa & Kamazaki 2011), adopting the method described by Takakuwa et al. (2007). Details of the ASTE observations and results are described by Takakuwa & Kamazaki (2011). Since the diameter of the ASTE telescope (= 10 m) is larger than the minimum projected baseline length of the SMA in its subcompact configuration ( $\sim 6.7 \text{ m}$ ), we were able to continuously sample the spatial scales from zero to  $\sim 200 \text{ k}\lambda$ . To assess whether the combining these two datasets introduces any systematic uncertainty, in Figure 1 we show the  $uv$ -distance and amplitude plot of the SMA and ASTE visibility datasets. The visibility amplitudes of the inner ASTE data smoothly connect with the outer SMA amplitudes, within the uncertainties of the absolute flux calibrations of  $\sim 20\%$  in both datasets, and thus combining the SMA and ASTE data does not introduce any additional uncertainty. To obtain the most optimum combined image cube of the envelope and the disk in L1551 IRS 5, we varied the number of the single-dish visibility sampling points and thus the relative ratio of the density of visibility points per unit  $uv$  area between the single-dish and the interferometric data. The ratio of 5 has been proposed as the most optimum ratio of the single-dish to interferometric visibility densities by Kurono et al. (2009) from their imaging simulations. In our images, we found that the density ratio of  $\sim 11$  provides the best compromise between the spatial

resolution and sensitivity and thus the most optimum combined image cube of the envelope and disk. The combined image cube recovers  $\sim 99\%$  of the total CS (7–6) flux density measured with ASTE at the spectral peak toward the field center while the SMA only image contains  $\sim 39\%$ , and the combined image cube can trace structures ranging from  $\lesssim 0''.9$  (combined synthesized beam) up to  $\sim 36''$  (SMA field of view) without a significant effect of the missing flux. In the following we discuss the structure and kinematics of the envelope and disk with the combined image cube adopting the ratio of 11. Table 1 summarizes the parameters of the present SMA observations and the SMA+ASTE image cube.

### 3. Results

#### 3.1. 343 GHz Continuum

Figure 2 shows the 343 GHz continuum image of L1551 IRS 5 taken with the SMA. Crosses in the image show the positions of the protobinary, which is taken from Lim & Takakuwa (2006). The continuum emission exhibits an elongated feature along the northwest to southeast direction, which is approximately perpendicular to the axes of the associated radio jets (blue and red arrows in Figure 2; Rodríguez et al. 2003). From the two-dimensional Gaussian fitting, the total flux density, beam-deconvolved size, and the position angle (P.A.) of the continuum emission are derived to be  $1.9 \pm 0.3$  Jy,  $160 \pm 10$  AU  $\times$   $80 \pm 10$  AU, and  $-23^\circ \pm 10^\circ$ , respectively. By comparison, the peak 850  $\mu$ m flux density observed with JCMT is  $3.16$  Jy beam $^{-1}$  at  $\sim 14''$  resolution (Moriarty-Schieven et al. 2006), and thus the continuum emission detected with the SMA contributes  $\sim 60\%$  of the total continuum flux. The peak position of the continuum emission derived from the Gaussian fitting is  $\sim 0''.3$  southeast from the position of the northern protostellar component as measured by Lim & Takakuwa (2006). In the L1551 region a global proper motion of  $\mu_\alpha = 0''.012 \pm 0''.002$  yr $^{-1}$  and  $\mu_\delta = -0''.023 \pm 0''.002$  yr $^{-1}$  has been identified (Jones & Herbig 1979; Rodríguez et al. 2003), which implies the present positions of the protobinary  $\sim +0''.07 \pm 0''.01$  east and  $\sim -0''.14 \pm 0''.01$  south from the nominal positions measured by Lim and Takakuwa (2006). The updated position of the northern protostar is still located  $\sim +0''.16$  north of the continuum peak position. On the other hand, the uncertainty of the peak position of the continuum emission measured from the Gaussian fitting is estimated to be  $\sim 0''.03$ , much smaller than the offset between the continuum peak and the protostellar positions. From these considerations, we suggest that the continuum peak is not associated with the northern or the southern protostar directly, and that the continuum emission most likely traces the flattened circumbinary+circumstellar disks (*e.g.*, Looney et al. 1997), embedded in the extended ( $\sim 1300$  AU) envelope component found with the JCMT observations. The ratio of the major and minor axes yields the disk inclination angle from the plane of the sky to be  $i = \cos^{-1}(\frac{80 \pm 10 \text{ AU}}{160 \pm 10 \text{ AU}}) = 60^\circ \pm 5^\circ$ .

The mass of the feature detected in the 343 GHz continuum ( $\equiv M_d$ ) was estimated as

$$M_d = \frac{S_\nu d^2}{\kappa_\nu B_\nu(T_d)}, \quad (1)$$

where  $\nu$  is the frequency,  $S_\nu$  the flux density,  $d$  the distance,  $B_\nu(T_d)$  the Planck function,  $T_d$  the dust temperature, and  $\kappa_\nu$  the dust opacity per unit gas + dust mass on the assumption of the gas-to-dust mass ratio of 100. The frequency dependence of  $\kappa_\nu$  is expressed as  $\kappa_\nu = \kappa_{\nu_0}(\nu/\nu_0)^\beta$ , where  $\beta$  denotes the dust-opacity index. The dust opacity of Ossenkopf & Henning (1994) for grains with thin ice mantles coagulated at a density of  $n_{H_2} \sim 10^6 \text{ cm}^{-3}$ ; *i.e.*,  $\kappa_{850 \text{ } \mu\text{m}} = 0.0182 \text{ cm}^2 \text{ g}^{-1}$ , was adopted. In L1551 IRS 5  $\beta = 1.0$  has been measured from the millimeter and submillimeter continuum data (Wu et al. 2009), and the measured value of  $T_d$  ranges from 47 K (Moriarty-Schieven et al. 1994) to 94 K (Kristensen et al. 2012), resulting in  $M_d = 0.032 - 0.070 M_\odot$ .

### 3.2. CS (7–6) Line

Figure 3 compares the ASTE, SMA, and the combined SMA + ASTE moment 0 maps of the CS (7–6) emission in L1551 IRS 5. The ASTE image shows an intense blob centered on the position of the protobinary with a possible extension toward the southwest ( $\sim 2500 \text{ AU}$ ), as already discussed by Takakuwa & Kamazaki (2011). The SMA-only CS image exhibits a  $\sim 300\text{-AU}$  scale, compact feature centered approximately on the protobinary, which is consistent with our earlier SMA results (Takakuwa et al. 2004). The combined SMA + ASTE image recovers the outskirts of the compact feature seen in the SMA-only image. In our previous study (Takakuwa & Kamazaki 2011), the SMA CS (7–6) data taken as the SMA early science study at a lower angular resolution ( $\sim 3''.2 \times 2''.0$ ) (Takakuwa et al. 2004) were combined with the ASTE image, and the combined image shows the central feature associated with the protobinary plus a weak diffuse component to the  $\sim 1500 \text{ AU}$  west and southwest of the protobinary. In our new combined SMA + ASTE image at a subarcsecond resolution, the structure of the central component associated with the protobinary is clearly resolved, while the brightness sensitivity becomes worse than the brightness temperature of the diffuse component. Hereafter in this paper, we will discuss the velocity structures of the material associated with the protobinary L1551 IRS 5, as detected with our new combined SMA + ASTE image cubes.

Figure 4 shows the SMA + ASTE velocity channel maps of the CS (7–6) line in L1551 IRS 5. The midpoint between the most extreme velocities is  $v_{\text{LSR}} = 6.6 \text{ km s}^{-1}$ , which is also the symmetric center of the Position-Velocity (P-V) diagrams (see Section 4). We therefore adopt  $v_{\text{LSR}} = 6.6 \text{ km s}^{-1}$  as the systemic velocity. In the high-velocity blueshifted region ( $3.8 \text{ km s}^{-1} - 5.0 \text{ km s}^{-1}$ ), a compact ( $\lesssim 2''$ ) CS emission is seen with its peak to the southeast of the protobinary. In the low-velocity blueshifted region ( $5.2 \text{ km s}^{-1} - 6.1 \text{ km s}^{-1}$ ), an extended CS emission with multiple peaks is seen, and the emission centroids appear to be located to the south of the protobinary. In the velocities close to the systemic velocity ( $6.3 \text{ km s}^{-1} - 6.8 \text{ km s}^{-1}$ ), both the blueshifted and redshifted emission are extended in the entire region. In the low-velocity redshifted region ( $7.0 \text{ km s}^{-1} - 7.9 \text{ km s}^{-1}$ ), an intense emission peak is seen to the west of the protobinary, whereas the overall emission centroids appear to be located to the north of the protobinary, which is opposite to the low-velocity blueshifted region. In the highly redshifted region ( $8.1 \text{ km s}^{-1} - 9.3 \text{ km s}^{-1}$ ),

a compact CS emission, just as in the case of the high-velocity blueshifted region, is seen to the north of the protobinary.

To better highlight the spatial-kinematic distributions of the CS emission, in Figure 5 we show the integrated-intensity maps in the high-velocity and low-velocity blueshifted and redshifted ranges separately, superposed on the 343 GHz dust continuum image. In the high-velocity range, the blueshifted and redshifted CS emission peaks are symmetrically located to the southeast and northwest with respect to the continuum peak. The position angle of the axis connecting the blueshifted and redshifted emission peaks matches that of the major axis of the 343 GHz continuum emission (dashed green line in Figure 5) within  $\sim 10^\circ$ , and the separation between the two peaks ( $\sim 140$  AU) is similar to the FWHM size of the 343 GHz continuum emission ( $\sim 160$  AU). Thus, the high-velocity CS emission exhibits a southeast (blue) to northwest (red) velocity gradient along the major axis of the circumbinary material as seen in the 343 GHz dust-continuum emission. In contrast, in the low-velocity range, the blueshifted and redshifted CS emission are extended and overlap with each other. The blueshifted emission peak is located to the south of the protobinary, while the redshifted emission peak is located to the west of the protobinary.

Figure 6 shows the intensity-weighted mean-velocity map of the CS emission in L1551 IRS 5. Along the major axis of the 343 GHz continuum emission (tilted vertical dashed line in Figure 6), the CS emission to the north of the protobinary is redshifted with the most redshifted velocity of  $7.8 \text{ km s}^{-1}$  at  $\sim 0.7''$  offset from the continuum peak, while the emission to the south is blueshifted with the most blueshifted velocity of  $5.4 \text{ km s}^{-1}$  at  $\sim 1.5''$ . This velocity feature reflects the velocity gradient seen in the high-velocity CS emission as shown in Figure 5. The global feature of the northern redshifted and southern blueshifted emission extends to the area outside of the continuum emission. We will discuss these velocity features with our simple models in the next section.

#### 4. Analyses

As shown in the previous section, the CS (7–6) emission surrounding L1551 IRS 5 exhibits distinct high-velocity and low-velocity features. The high-velocity emission comprises blueshifted and redshifted components located to the southeast and northwest, respectively, and as a whole the emission extent ( $\sim 160$  AU) and the position angle ( $\sim -30^\circ$ ) match with those of the compact continuum emission. The low-velocity components extend beyond the continuum-emission region up to  $\sim 1000$  AU, and the blueshifted and redshifted emission overlap with each other. Here, with our simple kinematical models we will interpret these results in the high-velocity and low-velocity regions separately. We adopt the peak position of the continuum emission as derived from the 2-dimensional Gaussian fitting as the center of the mass in these models.

#### 4.1. Central Compact CS Component: Keplerian Disk?

The high-velocity CS (7–6) emission immediately surrounding L1551 IRS 5 exhibits a clear velocity gradient along the northwest (red) – southeast (blue) direction. Since the direction of the velocity gradient is parallel to the major axis of the dust-continuum emission and the high-velocity CS emission traces the overall structure of the dust-continuum emission, a natural interpretation of the high-velocity CS emission is a rotating circumstellar disk. Recent interferometric observations of protostellar sources have been successfully modeling the circumstellar disks as geometrically-thin Keplerian disks (Tobin et al. 2012; Takakuwa et al. 2012; Takakuwa et al. 2013; Yen et al. 2013; Yen et al. 2014; Sakai et al. 2014). Recent theoretical simulations of disk formation have also shown that at  $\sim 100$ – $200$  AU scales the vertical extents of the disks are negligible ( $h \sim 20$  AU; Machida et al. 2011b). L1551 IRS 5 is associated with a 2500-AU scale flattened envelope seen in the  $\text{C}^{18}\text{O}$  (1–0) emission, with the position angle ( $\theta \sim -20^\circ$ ) and inferred inclination angle ( $i \sim 60^\circ$ ) similar to those of the compact ( $\sim 160$  AU) dust-continuum emission found with the present SMA observations. Thus, we performed model fittings of a geometrically-thin Keplerian disk to the high-velocity CS emission.

The procedure of the model fittings is basically the same as that adopted by Takakuwa et al. (2012). Since we assume that the disk is geometrically thin, the line-of-sight velocity at each position in right ascension and declination with respect to the disk center ( $\equiv v_{LOS}(\alpha, \delta)$ ) can be expressed as

$$v_{LOS}(\alpha, \delta) = v_{sys} + v_{rot}(r) \sin i \cos(\phi - \theta) + v_{rad}(r) \sin i \sin(\phi - \theta), \quad (2)$$

where

$$r = \sqrt{\left(\frac{x}{\cos i}\right)^2 + y^2}, \quad (3)$$

$$x = \alpha \cos(\theta) - \delta \sin(\theta), \quad (4)$$

$$y = \alpha \sin(\theta) + \delta \cos(\theta). \quad (5)$$

In the above expressions,  $v_{sys}$  is the systemic velocity,  $\theta$  is the position angle of the disk major axis,  $\phi$  is the azimuthal angle from the major axis on the disk plane,  $i$  is the disk inclination angle from the plane of the sky,  $\alpha$  and  $\delta$  are coordinates along right ascension and declination with respect to the disk center, and  $x$  and  $y$  are coordinates along the minor and major axes of the disk, respectively.  $v_{rot}(r)$  denotes the rotational velocity of the disk as a function of the radius ( $\equiv r$ ), and  $v_{rad}(r)$  is the radial velocity. In the case of Keplerian rotation,  $v_{rad}(r) = 0$  and  $v_{rot}(r)$  is expressed as

$$v_{rot}(r) = \sqrt{\frac{GM_\star}{r}}, \quad (6)$$

where  $G$  is the gravitational constant and  $M_\star$  is the mass of the central star. The 3-dimensional flux map of the CS emission, *i.e.*, the velocity channel maps, of the model disk ( $\equiv S_{model}(\alpha, \delta, v)$ )



can be expressed as

$$S_{model}(\alpha, \delta, v) = \left( S_{mom0}(\alpha, \delta) / \sigma \sqrt{2\pi} \right) \times \exp \left( \frac{-(v - v_{LOS}(\alpha, \delta))^2}{2.0\sigma^2} \right), \quad (7)$$

where  $S_{mom0}(\alpha, \delta)$  denotes the moment 0 map of the model disk and  $\sigma$  the internal velocity dispersion.

In our fitting, the moment 0 map of the model disk is assumed to be the same as the real observed moment 0 map (Figure 3 bottom-right). The purpose of our modeling is to investigate the velocity structure of the high-velocity CS emission, and to reproduce the observed velocity channel maps with kinematical and geometrical parameters. Even if the model moment 0 map is assumed to be the same as the observed moment 0 map, different kinematical parameters yield different velocities where the CS emission arises, and thus different model velocity channel maps. On the other hand, modeling the moment 0 map itself requires parameters of the profiles of surface density, temperature, and the molecular abundance, that is, parameters not related to the velocity structure. Therefore, to discuss the nature of the velocity structure our approach should be sufficient. To reduce the number of the fitting parameters, we fix the disk inclination angle  $i = -60^\circ$  derived from the ratio of the extents along the major and minor axes of the continuum emission, the systemic velocity of  $v_{sys} = 6.6 \text{ km s}^{-1}$ , and the velocity dispersion  $\sigma = 0.7 \text{ km s}^{-1}$  inferred from the inspection of the observed CS velocity channel maps. Only the high-velocity parts of the CS velocity channel maps ( $3.8 - 5.0 \text{ km s}^{-1}$  and  $8.1 - 9.3 \text{ km s}^{-1}$ ), which trace the structure of the continuum emission (see Figure 5 *left*), were included in the fitting. On these assumptions, we conducted minimum  $\chi^2$ -fittings of the velocity channel maps of the model Keplerian disk to the observed CS velocity channel maps, with  $M$  and  $\theta$  as fitting parameters;

$$\chi^2 = \sum_{\alpha, \delta, v} \left( \frac{S_{obs}(\alpha, \delta, v) - S_{model}^{M, \theta}(\alpha, \delta, v)}{\sigma_{rms}} \right)^2 \bigg/ \sum_{\alpha, \delta, v}, \quad (8)$$

where  $S_{obs}(\alpha, \delta, v)$  denotes the observed velocity channel maps,  $S_{model}^{M, \theta}$  the model velocity channel maps with given  $M_\star$  and  $\theta$ , and  $\sigma_{rms}$  the rms noise level of the observed velocity channel maps.

After running  $\sim 200$  sets of different parameters, we obtained the best-fit Keplerian-disk model, in which  $M_\star = 0.5_{-0.2}^{+0.6} M_\odot$  (which is equivalent to  $v_{rot} = 1.7_{-0.3}^{+0.9} \text{ km s}^{-1}$  at a radius  $r = 140 \text{ AU}$ ) and  $\theta = -33_{-24}^{+17}$  degrees. The error bars correspond to the  $\chi^2 + 1$  values. The middle and lower panels of Figure 7 show the velocity channel maps of the best-fit model and the residuals, respectively. Since the moment 0 map of the model Keplerian disk is assumed to be the same as the real observed moment 0 map, the model velocity channel maps do not exhibit perfectly smooth and symmetric features as expected from normal disk models. The residual velocity channel maps do not show any systematic features, and the rms of the residual maps is  $\sim 0.147 \text{ Jy beam}^{-1}$ , which is close to the noise level of the observed velocity channel maps ( $\sim 0.130 \text{ Jy beam}^{-1}$ ). The derived position angle of the Keplerian disk ( $\theta = -33^\circ$ ) is consistent with the major axis of the 343 GHz continuum emission ( $\theta = -23^\circ$ ), and approximately perpendicular to the axes of the jets driven

by the protobinary. We also fixed  $\theta = -23^\circ$  and performed another model fitting with  $M_\star$  as the only fitting parameter, and found that the best fit value of  $M_\star$  is still the same, with a slightly larger rms of the residual channel maps ( $\sim 0.149$  Jy beam $^{-1}$ ). As will be discussed in the next subsection, the radius of the 343 GHz continuum emission ( $\sim 160$  AU) is almost the same as the expected centrifugal radius derived from the outer envelope rotation and the central stellar mass derived from the present fitting. Furthermore, in the high-velocity regions of the fitting, the SMA-only image cube recovered at least  $\gtrsim 64\%$  of the ASTE flux. The model fitting to the SMA-only image cube in the same high-velocity regions provides a similar fitting result, with inclination angle  $i$  also as a fitting parameter ( $M_\star \sim 0.7 M_\odot$ ,  $\theta \sim -30^\circ$ , and  $i \sim -44^\circ$ ). These results show that the observed 343 GHz continuum emission and high-velocity CS emission are consistent with a Keplerian disk surrounding the L1551 IRS 5 binary system, or Keplerian circumbinary disk as in the case of L1551 NE (Takakuwa et al. 2012; Takakuwa et al. 2013). Interestingly, the estimated position and inclination angles of the circumbinary disk around L1551 IRS 5 are similar to those of the circumbinary disk around L1551 NE, but their rotations are in the opposite directions (in L1551 NE the northern part is blueshifted).

#### 4.2. Extended Component: Infalling Envelope with a Reduced Infalling Velocity?

While the high-velocity blueshifted and redshifted CS emission (Figure 5 *left*) are well reproduced by the Keplerian disk model, the low-velocity blueshifted and redshifted CS emission (Figure 5 *right*) appear to be distinct from the inner Keplerian disk. Momose et al. (1998) have found a  $\sim 2500$ -AU scale flattened envelope around L1551 IRS 5 in the C $^{18}$ O (1–0) emission with the NMA, which exhibits infalling and rotating gas motion with a conserved specific angular momentum. The rotational velocity with a conserved specific angular momentum is expressed as,

$$v_{rot}(r) = \frac{j}{r}, \quad (9)$$

where  $j$  denotes the specific angular momentum. Momose et al. (1998) measured  $j \sim 168$  AU km s $^{-1}$  in the flattened C $^{18}$ O envelope around L1551 IRS 5. Equating eq. (6) and eq. (9) provides the transitional radius from the outer infalling envelope to the inner Keplerian disk. For  $M_\star = 0.5 M_\odot$  and  $j = 168$  AU km s $^{-1}$ , the outermost Keplerian radius is calculated to be  $r_{kep} \sim 64$  AU or 128 AU in diameter, which is almost the same as the FWHM size of the continuum emission ( $\sim 160$  AU). This means that the outer rotation of the infalling envelope seen in the C $^{18}$ O (1–0) emission naturally connects to the rotation of the Keplerian circumbinary disk as traced by the high-velocity CS emission and the dust-continuum emission. The low-velocity CS (7–6) emission we observed with the SMA and ASTE may trace the innermost part of this infalling envelope.

Figure 8 (upper panels) shows the observed Position-Velocity (P-V) diagrams of the CS (7–6) emission in L1551 IRS 5 along the major (*left*) and minor axes (*right*) of the Keplerian disk identified by the high-velocity CS emission. In the P-V diagrams, horizontal dashed lines delineate

the size of the Keplerian disk, and vertical dashed lines the velocity borderlines used to separate the high-velocity and low-velocity components. In the observed P-V diagram along the major axis, the velocity gradient along the southeast (blueshifted) to the northwest (redshifted) direction is evident both within and outside of the Keplerian-disk region. The lower-velocity emission outside of the Keplerian disk extends to  $r \sim 500$  AU, while the higher-velocity emission originated from the Keplerian disk is located closer to the central protobinary. To contrast the velocity feature of the outer lower-velocity emission with that of the inner Keplerian disk, curves of two kinds of rotations are drawn in the P-V diagram along the major axis. One is the rotation with the conserved angular momentum derived from the  $\text{C}^{18}\text{O}$  envelope by Momose et al. (1998) (*i.e.*, eq. (9) with  $j = 168$  AU km s $^{-1}$ ; red curves in Figure 8). The other is the Keplerian rotation derived in the previous subsection (*i.e.*, eq. (6) with  $M_\star = 0.5_{-0.2}^{+0.6} M_\odot$ ; green, blue, and purple curves in Figure 8). Although the Keplerian and  $r^{-1}$  rotation curves are almost indistinguishable in the higher-velocity parts, the  $r^{-1}$  rotation curve with  $j = 168$  AU km s $^{-1}$ , which reproduces the rotation of the  $\text{C}^{18}\text{O}$  envelope, appears to better trace the velocity feature of the lower-velocity CS emission. Hereafter we fix  $j = 168$  AU km s $^{-1}$  for the rotation traced by the low-velocity CS emission.

In the P-V diagram along the minor axis, the higher-velocity parts do not exhibit any clear velocity gradient, as expected from the Keplerian rotation. On the other hand, the lower-velocity CS emission shows that in the northeastern part the CS emission is primarily redshifted while in the southwestern part both the blueshifted and redshifted CS emission are seen. Thus, there is a possible northeast (red) to southwest (blue) velocity gradient in the lower-velocity CS emission. Since the associated bipolar outflows are also blueshifted to the southwest and redshifted to the northeast (Moriarty-Schieven et al. 2006; Wu et al. 2009), a possible interpretation for the low-velocity components is a molecular outflow. If the low-velocity CS components indeed trace the associated molecular outflow, then based on their projected velocity with respect to the systemic velocity and the projected separation from the protobinary along the minor axis ( $\lesssim 0.5$  km s $^{-1}$  and  $\sim 1'' \sim 140$  AU, respectively), and assuming that the outflow emerges perpendicular to the Keplerian disk, the deprojected outflow velocity is estimated to be  $v_{flow} \sim 0.5$  km s $^{-1} / \cos i \sim 1$  km s $^{-1}$ , and the deprojected separation  $l_{flow} \sim 140$  AU /  $\sin i \sim 162$  AU. By comparison, at a given separation from the central gravity source the escape velocity ( $\equiv v_g$ ) is

$$v_g = \sqrt{\frac{2GM_\star}{l_{flow}}}. \quad (10)$$

Since  $M_\star$  is derived to be  $0.5 M_\odot$  from the Keplerian rotation, we find  $v_g \sim 2.3$  km s $^{-1}$ , a factor of 2 higher than the deprojected outflow velocity estimated above ( $v_{flow} \sim 1$  km s $^{-1}$ ). The low-velocity components are therefore bound to the protostellar system. Furthermore, contrary to expectations for a molecular outflow driven along the northeast to southwest direction, the low-velocity components are widely distributed and do not show any bipolar feature. Thus, it is unlikely that the low-velocity components originate from the associated molecular outflow.

Instead, the northeast (red) to southwest (blue) velocity gradient in the low-velocity CS emission may trace the infalling motion toward the central Keplerian disk in the flattened protostellar

envelope. Since the associated bipolar outflows are blueshifted to the southwest and redshifted to the northeast (Moriarty-Schieven et al. 2006; Wu et al. 2009), the near-side of the flattened envelope is northeast and the far-side southwest, and the redshifted emission on the near-side and the blueshifted emission on the far-side imply infalling motion in the envelope. Assumption of the flattened morphology of the CS emission is probably valid, since at  $r \sim 500$  AU the expected scale height of the flared disk / envelope is  $\lesssim 50$  AU (Machida et al. 2014), and Momose et al. (1998) successfully modeled the  $\sim 2500$ -AU scale envelope seen in the  $\text{C}^{18}\text{O}$  (1–0) emission as a flattened infalling and rotating envelope. To quantitatively understand the infalling motion, in the P-V diagram along the minor axis we draw curves expected from the free-fall motion expressed as;

$$v_{rad}(r) = \sqrt{\frac{2GM_{\star}}{r}}. \quad (11)$$

From our Keplerian model fitting to the high-velocity CS emission, the central stellar mass is estimated to be  $\sim 0.5_{-0.2}^{+0.6} M_{\odot}$ . The blue, purple, and green curves in Figure 8 show the infalling curves with the central stellar mass derived from the Keplerian fitting and its upper and lower ends, respectively. It is evident that the free-falling curves with the best-fit value  $M_{\star} = 0.5 M_{\odot}$ , and even with the lower end ( $M_{\star} = 0.3 M_{\odot}$ ), do not trace the emission ridge in the P-V diagram along the minor axis. If, for example, we reduce the central stellar mass by one order of magnitude to  $0.05 M_{\odot}$ , the infalling curves (cyan curves in Figure 8) trace the bulk of the CS emission ridge much better. These results show that the infalling motion, if any,

To reproduce the low-velocity CS emission as the rotating and infalling flattened envelope with the same rotational profile as that of the outer  $\text{C}^{18}\text{O}$  envelope and the slower inward motion than the free-fall motion, we have generated a toy model of a geometrically-thin disk with velocity fields described by

$$v_{rot}(r) = \sqrt{\frac{GM_{\star}}{r}}, v_{rad}(r) = 0 \quad (\text{Keplerian region}), \quad (12)$$

$$v_{rot}(r) = \frac{j}{r}, v_{rad}(r) = \sqrt{\frac{2GM_{\star}^{inf}}{r}} \quad (\text{infalling region}), \quad (13)$$

where  $M_{\star}^{inf}$  denotes the reduced central stellar mass to reproduce the infalling velocity. As in the case of the Keplerian-disk fitting described in the last subsection, the two-dimensional intensity distribution of the model disk was taken to be the same as the observed CS moment 0 map. Asymmetric or clumpy features in the model velocity channel maps or P-V diagrams thus originate from the observed CS moment 0 map. To separate the inner Keplerian region from the outer infalling region, we defined the area within the FWHM of the Gaussian fit of the continuum emission as the Keplerian region, and the area outside as the infalling region. Based on the results of the  $\chi^2$  model fitting to the high-velocity CS emission, we adopted  $M_{\star} = 0.5 M_{\odot}$ ,  $v_{sys} = 6.6 \text{ km s}^{-1}$ ,  $i = 60^{\circ}$ ,  $\theta = -33^{\circ}$ , and  $\sigma_{gas} = 0.7 \text{ km s}^{-1}$ . The specific angular momentum  $j = 168 \text{ AU km s}^{-1}$  and  $M_{\star}^{inf} = 0.05 M_{\odot}$  are also adopted from previous discussions. With these parameters, we created the model velocity channel maps with the same procedure as that described in the last subsection,

and then the model P-V diagrams, which are shown in Figure 8 (*lower panels*). The model P-V diagrams well reproduce the observed velocity structures. Along the major axis, the model P-V diagram shows both the high-velocity Keplerian rotation part and the low-velocity envelope part with the  $r^{-1}$  rotation. The model P-V diagram along the minor axis shows that there is no velocity gradient in the high-velocity Keplerian part, while in the low-velocity part the velocity gradient caused by the slow infalling motion is evident. Figure 9 compares the observed and model velocity channel maps in the low-velocity region. For the velocities of  $5.3 - 6.0 \text{ km s}^{-1}$  and  $7.1 - 7.8 \text{ km s}^{-1}$ , the positions of the emission centroids of the model channel maps are located to the south and north of the protobinary, respectively, and the position angle of the axis connecting between the blueshifted and redshifted components is  $\sim 0^\circ$ , different from the position angle of the major axis of the high-velocity Keplerian disk component. This is because both the rotational and infalling motions in the envelope contribute to the observed velocities, as expressed in eq. (2). Although the observed velocity channel maps show multiple emission peaks, the overall trend of the emission centroids in these velocities is consistent with that of our model. Around the systemic velocities ( $6.4 - 6.7 \text{ km s}^{-1}$ ), the model channel maps show that the CS emission is extended on both the northern and southern sides with eastern and western emission peaks. The observed velocity channel maps in these velocities also show that the CS emission is extended in both the northern and southern sides, although the eastern emission peaks seen in the model channel maps are not clear in the observed velocity channel maps. These results suggest that the observed velocity structures in the lower-velocity region can be interpreted as a rotating and infalling envelope, which has a rotational profile with the conserved angular momentum and the infalling speed slower than that expected from the free-fall onto the central stellar mass of  $0.5 M_\odot$ .

By contrast, the high-velocity CS emission is unlikely to trace the same envelope kinematic component. We performed  $\chi^2$  model fitting of the rotating and infalling envelope to the high-velocity CS emission, which is expressed by eq. (13), with  $M_\star^{inf}$ ,  $j$  and  $\theta$  as fitting parameters, and fixed  $v_{sys} = 6.6 \text{ km s}^{-1}$ ,  $i = 60^\circ$ , and  $\sigma_{gas} = 0.7 \text{ km s}^{-1}$ . The best-fit result of the rotating and infalling envelope model to the high-velocity CS emission is  $M_\star^{inf} = 8.0 \times 10^{-6} M_\odot$ ,  $j = 250 \text{ AU km s}^{-1}$ , and  $\theta = -40^\circ$ , which corresponds to  $v_{rad} = 0.01 \text{ km s}^{-1}$  and  $v_{rot} = 1.8 \text{ km s}^{-1}$  at  $r = 140 \text{ AU}$ . This result is unphysical because this mass is too small for a typical Class I protostar, and previous studies on the orbital motion of L1551 IRS 5 with VLA show the total mass  $\sim 0.9 M_\odot$  (Lim & Takakuwa 2006). In fact this fitting result demonstrates that there is little infall, which means the motion is essentially Keplerian, and thus our interpretation of the Keplerian disk is more straightforward to reproduce the observed velocity feature of the high-velocity CS emission.

In summary, the submillimeter CS emission in L1551 IRS 5 traces primarily two distinct components; one is an  $r \sim 64 \text{ AU}$ -scale Keplerian circumbinary disk, and the other an extended ( $r \sim 500 \text{ AU}$ ) rotating and infalling envelope with the  $r^{-1}$  rotational profile and reduced infalling speed. In the next section, we will discuss these results in the context of disk formation from protostellar envelopes and evolution of disks around protostellar sources.

## 5. Discussion

### 5.1. Keplerian Disk Embedded in the Infalling Envelope around L1551 IRS 5

As described in the previous section, our SMA + ASTE observations of the Class I protostellar binary L1551 IRS 5 in the 343 GHz continuum and CS (7–6) line have revealed an  $r \sim 64$  AU-scale Keplerian disk with a mass of  $\sim 0.070 M_{\odot}$  around the central protobinary mass of  $\sim 0.5 M_{\odot}$ , which is embedded in a rotating and infalling envelope. The observed rotational profile in the infalling envelope is consistent with rotation with the conserved angular momentum found in the outer ( $r \sim 1200$  AU) envelope (*i.e.*, eq. (9); Momose et al. 1998), and connects to the inner Keplerian rotation. On the other hand, the observed infalling velocity is clearly lower than the free-fall velocity onto the central protobinary mass of  $0.5 M_{\odot}$ , which is derived from the observed Keplerian rotation in the disk. We consider that these results reveal the transition from the infalling envelope to the Keplerian disk.

Although it is not straightforward to form Keplerian disks from infalling envelopes because of the efficient magnetic braking (Mellon & Li 2008; Mellon & Li 2009; Machida et al. 2011a; Machida et al. 2011b; Li et al. 2011), the latest theoretical simulations (Machida et al. 2014) successfully produced Keplerian disks with properties similar to those found by the previous and present observations. They argued that the outcome of their simulations highly depends on the initial model settings such as the sink accretion radius and the initial core density structure (uniform or Bonnor-Ebert sphere). For their small sink accretion radii ( $r_{acc} \lesssim 1$  AU), they produced  $r \sim 50$ – $100$  AU Keplerian disks with masses of  $\sim 0.06$ – $0.15 M_{\odot}$  embedded within  $r \sim 1000$ -AU scale flattened envelopes, when the central protostellar masses reach  $\sim 0.5 M_{\odot}$ . In the outer region ( $r \gtrsim 200$  AU) the envelope rotation approximately follows the  $r^{-1}$  profile that connects to the inner Keplerian rotation. In the intermediate region ( $50$ – $100$  AU  $\leq r \leq 200$  AU), the decrease in the infalling speed is also reproduced, as the matter approaches the centrifugal radius. At the stage of the formation of  $r \sim 50$ – $100$  AU Keplerian disks, substantial envelope masses ( $\sim 1 M_{\odot}$ ) still remain. Furthermore, the morphology of the infalling envelopes at  $r \sim 1000$  AU scale is flattened with the typical scale height of  $100$ – $200$  AU (Machida et al. 2014). These results show that our observational results in L1551 IRS 5, as well as those of the C<sup>18</sup>O (1–0) emission (Momose et al. 1998), can be reproduced by the latest theoretical simulations.

The picture of the transition from the infalling envelope to the Keplerian disk shows certain similarities among different sources. In the case of L1551 NE, another Class I protobinary source located  $\sim 2'.5$  northwest of L1551 IRS 5, Takakuwa et al. (2013) have found that the infalling velocity is much smaller than the free-fall velocity toward the central stellar mass of  $0.8 M_{\odot}$  derived from the Keplerian rotation. The reduction of the infalling velocities is also found in a Class 0/I protostar L1527 IRS (Ohashi et al. 2014) and a Class I protostar TMC-1A (Aso et al. in prep) from ALMA Cycle 0 observations. On the other hand, the observed lower angular momentum of the infalling gas than that of the central disk in L1551 NE is essentially different from the result of L1551 IRS 5. As discussed by Takakuwa et al. (2013), in the case of L1551 NE the magnetic braking may

be efficient in the envelope region but inefficient in the disk due to the higher plasma  $\beta$ , the ratio of the gas thermal pressure to the magnetic pressure. Around a Class I protostar L1489 IRS, Yen et al. (2014) have identified free-falling gas with the rotational angular momentum consistent with that of the outer boundary of the Keplerian disk. In the case of L1489 IRS the amount of the surrounding envelope is much smaller ( $\sim 0.02 M_{\odot}$ ) than that of L1551 IRS 5 and L1551 NE, and thus the free-falling gas component may be a remnant gas component falling toward the central disk. Accumulation of more examples of the transitions from infall to Keplerian rotation is needed to draw a more general picture of disk formation from protostellar envelopes. Furthermore, the transitional regions from the infalling envelopes to the Keplerian disks are expected to be at  $r \sim 100\text{--}300$  AU. To fully resolve such size scales, higher-resolution observations at  $\sim 10$  AU are needed. Forthcoming ALMA observations of protostellar envelopes should be able to achieve this goal.

## 5.2. Evolution of Keplerian Disks around Protostars

Our observations of L1551 IRS 5 unveiled a Keplerian disk around the protobinary embedded in the infalling envelope. Since the mass of the entire envelope around L1551 IRS 5 derived from the single-dish  $850 \mu\text{m}$  mapping is  $\sim 1 M_{\odot}$  (Moriarty-Schieven et al. 2006) and thus larger than the disk ( $\sim 0.070 M_{\odot}$ ) + protobinary ( $\sim 0.5 M_{\odot}$ ) masses, further growth of the central protobinary + disk system through the mass accretion from the envelope is expected. On the assumption that the high-velocity CS emission (Figure 5 *left*) traces the same disk component as that traced by the 343 GHz continuum emission, and that the CS emission is in the LTE condition with the excitation temperature of 47 K (Moriarty-Schieven et al. 1994), we derived the CS abundance to be  $\sim 1.6 \times 10^{-8}$ . Applying this abundance to the low-velocity CS emission (Figure 5 *right*) yields the envelope mass of  $\sim 0.38 M_{\odot}$ . The typical mean radius of the envelope component is  $\sim 3''.5$ , and the infalling velocity at that radius is  $\sim 0.43 \text{ km s}^{-1}$ , providing the infalling time of  $\sim 5400 \text{ yr}$  and thus the mass accretion rate of  $\sim 7.0 \times 10^{-5} M_{\odot} \text{ yr}^{-1}$ . On the other hand, the mass outflowing rate has been estimated to be  $\sim 1 \times 10^{-6} M_{\odot} \text{ yr}^{-1}$  by Liseau et al. (2005). Therefore, the envelope material can further accrete onto the central system during the typical Class I period of  $2.5 - 6.7 \times 10^5 \text{ yr}$  (Hatchell et al. 2007).

Recent high-resolution interferometric observations have been finding more and more Keplerian circumstellar disks around protostellar sources embedded in protostellar envelopes (Brinch et al. 2007; Lommen et al. 2008; Jørgensen et al. 2009; Tobin et al. 2012; Yen et al. 2013; Harsono et al. 2014). Our previous SMA observations of L1551 NE have identified an  $r \sim 300\text{-AU}$  scale Keplerian disk with a central stellar mass of  $0.8 M_{\odot}$  (Takakuwa et al. 2012; Takakuwa et al. 2013), embedded in an envelope with the mass of  $\sim 0.4 M_{\odot}$  (Moriarty-Schieven et al. 2006). With ALMA, more deeply embedded Keplerian disks are found around Class 0 protostars such as VLA 1623A, HH 212, and L1527 IRS (Murillo et al. 2013; Lee et al. 2014; Ohashi et al. 2014). Yen et al. (2013) investigated the evolutionary sequence of protostellar envelopes into Keplerian-disk formation, based upon their

SMA survey of protostellar envelopes, as well as previously published results. They found that gas motions in the protostellar envelopes can be categorized into three types; (1) no detectable rotation but infalling motion around early Class 0 protostars; (2)  $v_{rot} \sim r^{-1}$  rotational motion in the infalling envelopes around late Class 0 and early Class I sources; and (3) large-scale Keplerian disks around Class I protostars. They proposed that the differences of the envelope gas motions reflect evolutionary trends of the protostellar envelopes into the Keplerian-disk formation. L1551 IRS 5 is classified in category (2) in their paper, but our new higher-resolution observations unveiled the Keplerian disk embedded in the infalling envelope. These results imply that Keplerian circumstellar disks with size scales comparable to those around T-Tauri stars are present at the protostellar stages still deeply embedded in protostellar envelopes, and that Keplerian-disk formation should occur in the late Class 0 or early Class I stages.

To discuss the evolutionary sequence of Keplerian disks around protostellar sources after their formation, in Table 2 we compile the measured physical properties of the protostars and the associated Keplerian disks, including those of L1551 IRS 5, sorted by the bolometric temperature ( $T_{bol}$ ). As another evolutionary indicator, we also list the ratio of the central protostellar mass to the total star+disk+envelope mass ( $\equiv \frac{M_{\star}}{M_{\star}+M_{disk}+M_{env}}$ ) in Table 2. The mass ratio of L1551 IRS 5 is the lowest among the Class I sources, and that of the two Class 0 sources are the lowest among the entire sample as expected. However, there is no clear distinction of the radii and masses of the Keplerian disks between these early protostellar sources and the other, more evolved protostars. These results suggest that the Keplerian disks do not grow much after the disks become hundreds AU scales at the late Class 0 or early Class I stages. In contrast, the positive trend of the ratio of the central protostellar mass to the total star+disk+envelope mass with  $T_{bol}$  implies further growth of the central protostellar masses with respect to the envelope masses. The Keplerian disks may be in a quasi-static mode of mass accretion onto the protostars, or episodic mass accretions from the disks onto the central protostars may be ongoing, as proposed from Spitzer survey observations of protostellar sources (Dunham et al. 2008). Theoretical simulations by Machida & Hosokawa (2013) and Machida et al. (2014) show that the mass of the Keplerian disk does not grow much and saturates at  $\sim 0.06\text{--}0.15 M_{\odot}$  after the large-scale  $r \sim 50\text{--}100$  AU Keplerian disk appears, while the mass of the central protostar keeps growing from  $\sim 0.5 M_{\odot}$  to  $\sim 1.0 M_{\odot}$ . In the innermost part of the disk ( $r \lesssim 30$  AU) mass accretion toward the central protostar is reproduced because of the slow angular momentum transfer by the outflows. Thus, these theoretical simulations are at least qualitatively consistent with the observed evolutionary properties of the Keplerian disks around the protostellar sources.

The Keplerian disk around L1551 IRS 5 is a circumbinary disk surrounding a protostellar binary system. Since the radius of the Keplerian circumbinary disk is  $\sim 64$  AU and the projected binary separation  $\sim 40$  AU, dynamical interaction between the circumbinary disk and the protobinary is anticipated. In the more evolved (T-Tauri) binary GG Tau (projected separation  $\sim 35$  AU), a ringlike feature of the circumbinary disk, where the innermost part of the disk ( $r \lesssim 200$  AU) has been cleared by the dynamical interaction with the binary stars, is identified



(Guilloteau et al. 1999; Andrews et al. 2014). Recently, such a ringlike feature is also identified in a protostellar binary L1551 NE with ALMA by Takakuwa et al. (2014). The observed ringlike structure and the gas motion in the circumbinary disk of L1551 NE can be reproduced with spiral-arm features and rotating and accreting gas motions toward the protostellar binary, caused by the gravitational torques from the binary protostars. The spatial resolution of the present SMA observations of L1551 IRS 5 ( $\sim 100$  AU) is, however, not high enough to separate the circumbinary ring from the circumstellar disks around the individual stars and investigate whether the dynamical interaction between the circumbinary disk and the binary is present or not. Further higher-resolution observations of L1551 IRS 5 will unveil the presence/absence of such a dynamical interaction in this protostellar binary system.

## 6. Summary

We have carried out sub-arcsecond resolution SMA observations of the protobinary system L1551 IRS 5 in the 343 GHz continuum and the CS (7–6) line. The SMA data in the CS (7–6) line are combined with the ASTE single-dish data to fill in the missing short spacing information, and the combined image cube is discussed with our simple kinematical models. The main results are summarized below:

1. The 343 GHz dust-continuum emission in L1551 IRS 5 shows an intense central peak associated with the protobinary with an elongated feature along the northwest to southeast direction ( $160 \pm 10$  AU  $\times$   $80 \pm 10$  AU, P.A. =  $-23^\circ \pm 10^\circ$ ), which is perpendicular to the associated binary jets. The continuum emission most likely traces the circumbinary material, and the mass of the circumbinary material is estimated to be  $\sim 0.070 M_\odot$ .

2. The combined SMA + ASTE moment 0 map of the CS emission in L1551 IRS 5 shows a  $\sim 1000$  AU-scale feature with its peak close to the protobinary. The CS velocity channel maps reveal that the velocity structures can be decomposed into two components. One is a high-velocity ( $\gtrsim 1.5$  km s $^{-1}$ ), compact blueshifted and redshifted emission located to the southeast and northwest of the protobinary, respectively, which traces the structure of the circumbinary material seen in the 343 GHz dust-continuum emission and exhibits the velocity gradient along the major axis of the continuum emission. The other is a low-velocity ( $\lesssim 1.3$  km s $^{-1}$ ), extended blueshifted and redshifted emission, that exhibits a slight south (blueshifted) to north (redshifted) emission offset, but shows emission overlaps.

3.  $\chi^2$  model fitting of geometrically-thin Keplerian disks to the 3-dimensional image cube of the high-velocity CS emission was performed. The channel maps of the high-velocity CS emission are well-reproduced by a geometrically-thin Keplerian disk model with the central stellar mass  $M_\star = 0.5^{+0.6}_{-0.2} M_\odot$  and the disk position angle  $\theta = -33^{+17}_{-24}^\circ$ , where the disk inclination angle  $i = -60^\circ$  and the internal velocity dispersion  $\sigma = 0.7$  km s $^{-1}$  are fixed. The extent and the major axis of the best-fit Keplerian disk model match well with those of the 343 GHz continuum emission. These

results show that both the high-velocity CS emission and the 343 GHz dust-continuum emission trace a Keplerian disk around the protobinary.

4. The observed velocity features of the low-velocity CS emission component can be reproduced with a model of the flattened rotating and infalling envelope. The rotational profile is consistent with the rotation of the conserved angular momentum deduced from the previous C<sup>18</sup>O (1–0) observations (*i.e.*,  $v_{rot} = \frac{j}{r}$ ;  $j = 168 \text{ AU km s}^{-1}$ ), and connects smoothly to the inner Keplerian rotation at a radius of  $\sim 64 \text{ AU}$ , which is consistent with the radius of the 343 GHz continuum emission. The derived infalling velocity is 3 times smaller than the free-fall velocity (10 times smaller in terms of the central stellar mass) toward the central stellar mass of  $0.5 M_{\odot}$  as estimated from the Keplerian rotation, suggesting that the infall velocity is reduced as the matter approaches close to the centrifugal radius. We suggest that these results demonstrate the transition from the outer infalling envelope to the inner Keplerian disk.

5. The latest theoretical models of disk formation from protostellar envelopes can reproduce the main characteristic features of the observed transition from the infalling envelope to the inner Keplerian disk in L1551 IRS 5, including the disk radius ( $\sim 64 \text{ AU}$ ), mass of the central object ( $\sim 0.5 M_{\odot}$ ), disk ( $\sim 0.070 M_{\odot}$ ), and the envelope ( $\sim 1 M_{\odot}$ ), and the  $v_{rot} \sim r^{-1}$  rotational profile and the reduced infalling speed in the envelope. Compilation of protostellar sources associated with Keplerian disks shows that the Keplerian disks do not grow much once they become large enough to be observable ( $r \gtrsim 50\text{--}200 \text{ AU}$ ) at the late Class 0 or the early Class I stages, while the central protostars appear to keep growing through mass accretion. These results indicate that the Keplerian disks around the protostars keep supplying materials to the central objects, whereas the disks themselves do not grow. These results are also consistent with the latest theoretical models of disk formation, which show saturation of the masses of the Keplerian disks at around  $\sim 0.06\text{--}0.15 M_{\odot}$  after the disks grow to large scales ( $r \sim 50\text{--}100 \text{ AU}$ ), while the masses of the central protostars keep growing from  $\sim 0.5 M_{\odot}$  to  $\sim 1.0 M_{\odot}$  through the mass supply from the innermost part of the disks.

We are grateful to J. Lim, M. Momose, M. Saito, and Zhi-Yun Li for their fruitful discussions, and an anonymous referee for helpful suggestions. We would like to thank all the SMA staff supporting this work. S.T. acknowledges a grant from the National Science Council of Taiwan (MOST 102-2119-M-001-012-MY3) in support of this work.

## REFERENCES

- Andrews, S. M., & Williams, J. P. 2005, *ApJ*, 631, 1134
- Andrews, S. M., & Williams, J. P. 2007, *ApJ*, 671, 1800
- Andrews, S. M., Chandler, C. J., Isellar, A., et al. 2014, *ApJ*, 787, 148
- Brinch, C., Crapsi, A., Jørgensen, J. K., Hogerheijde, M. R., & Hill, T. 2007, *A&A*, 475, 915
- Dunham, M. M., Crapsi, A., Evans II, N. J., Bourke, T. L., Huard, T. L., Myers, P. C., & Kauffmann, J. 2008, *ApJS*, 179, 249
- Eisner, J. A. 2012, *ApJ*, 755, 23
- Froebrich, D. 2005, *ApJS*, 156, 169
- Guilloteau, S., & Dutrey, A. 1998, *A&A*, 339, 467
- Guilloteau, S., Dutrey, A., & Simon, M. 1999, *A&A*, 348, 570
- Hara, C., Shimajiri, Y., Tsukagoshi, T., Kurono, Y., Saigo, K., Nakamura, F., Saito, M., Wilner, D. J., & Kawabe, R. 2013, *ApJ*, 771, 128
- Harsono, D., Jørgensen, J. K., van Dishoeck, E. F., Hogerheijde, M. R., Bruderer, S., Persson, M. V., & Mottram, J. C. 2013, *A&A*, 562, 77
- Hatchell, J., Fuller, G. A., Richer, J. S., Harries, T. J., & Ladd, E. F. 2007, *A&A*, 468, 1009
- Ho, P. T. P., Moran, J. M., & Lo, K. Y. 2004, *ApJ*, 616, L1
- Jones, B. F., & Herbig, G. H. 1979, *AJ*, 84, 1872
- Jørgensen, J. K., van Dishoeck, E. F., Visser, R., Bourke, T. L., Wilner, D. J., Lommen, D., Hogerheijde, M. R., & Myers, P. C. 2009, *A&A*, 507, 861
- Kenyon, S. J., Dobrzycka, D., & Hartmann, L. 1994, *AJ*, 108, 1872
- Kristensen, L. E., van Dishoeck, E. F., et al. 2012, *A&A*, 542, 8
- Kurono, Y., Morita, K.-I., & Kamazaki, T. 2009, *PASJ*, 61, 873
- Lee, C.-F., Hirano, N., Zhang, Q., Shang, H., Ho, P. T. P., & Krasnopolsky, R. 2014, *ApJ*, 786, 114
- Li, Z.-Y., Krasnopolsky, R., & Shang, H. 2011, *ApJ*, 738, 180
- Lim, J., & Takakuwa, S. 2006, *ApJ*, 653, 425
- Liseau, R., Fridlund, C. V. M., & Larsson, B. 2005, *ApJ*, 619, 959

- Lommen, D., Jørgensen, J. K., van Dishoeck, E. F., & Crapsi, A. 2008, *A&A*, 481, 141
- Looney, L. W., Mundy, L. G., & Welch, W. J. 1997, *ApJ*, 484, L157
- Machida, M. N., & Matsumoto, T. 2011a, *MNRAS*, 413, 2767
- Machida, M. N., Inutsuka, S.-I., & Matsumoto, T. 2011b, *PASJ*, 63, 555
- Machida, M. N., & Hosokawa, T. 2013, *MNRAS*, 431, 1719
- Machida, M. N., Inutsuka, S.-I., & Matsumoto, T. 2014, *MNRAS*, 438, 2278
- Mellon, R. R., & Li, Z.-Y. 2008, *ApJ*, 681, 1356
- Mellon, R. R., & Li, Z.-Y. 2009, *ApJ*, 698, 922
- Momose, M., Ohashi, N., Kawabe, R., Nakano, T., & Hayashi, M. 1998, *ApJ*, 504, 314
- Moriarty-Schieven, G. H., Wannier, P. G., Keene, J., & Tamura, M. 1994, *ApJ*, 436, 800
- Moriarty-Schieven, G. H., Johnstone, D., Bally, J., & Jenness, T. 2006, *ApJ*, 645, 357
- Murillo, N. M., Lai, S.-P., Bruderer, S., Harsono, D., & van Dishoeck, E. F. 2013, *A&A*, 560, A103
- Ohashi, N., Hayashi, M., Kawabe, R., & Ishiguro, M. 1996, *ApJ*, 466, 317
- Ohashi, N., Hayashi, M., Ho, P. T. P., Momose, M., Tamura, M., Hirano, N., & Sargent, A. I. 1997, *ApJ*, 488, 317
- Ohashi, N., Saigo, K., Aso, Y., et al. 2014, *ApJ*, in press
- Ossenkopf, V., & Henning, T. 1994, *A&A*, 291, 943
- Rodríguez, L. F., D’Alessio, P., Wilner, D. J., Ho, P. T. P., Torrelles, J. M., Curiel, S., Gómez, Y., Lizano, S., Pedlar, A., Cantó, J., & Raga, A. C. 1998, *Nature*, 395, 355
- Rodríguez, L. F., Porras, A., Claussen, M. J., Curiel, S., Wilner, D. J., & Ho, P. T. P. 2003, *ApJ*, 586, L137
- Saito, M., Kawabe, R., Kitamura, Y., & Sunada, K. 1996, *ApJ*, 473, 464
- Sakai, N., Sakai, T., et al. 2014, *Nature*, 507, 78
- Schaefer, G. H., Dutrey, A., Guilloteau, S., Simon, M., & White, R. J. 2009, *ApJ*, 701, 698
- Scoville, N. Z., Carlstrom, J. E., Chandler, C. J., Phillips, J. A., Scott, S. L., Tilanus, R. P. J., & Wang, Z. 1993, *PASP*, 105, 1482
- Simon, M., Dutrey, A., & Guilloteau, S. 2000, *ApJ*, 545, 1034

- Takakuwa, S., Ohashi, N., & Hirano, N. 2003, *ApJ*, 590, 932
- Takakuwa, S., Ohashi, N., Ho, P. T. P., Qi, C., Wilner, D. J., Zhang, Q., Bourke, T. L., Hirano, N., Choi, M., & Yang, J. 2004, *ApJ*, 616, L15
- Takakuwa, S., Ohashi, N., Bourke, T. L., et al. 2007, *ApJ*, 662, 431
- Takakuwa, S., & Kamazaki, T. 2011, *PASJ*, 63, 921
- Takakuwa, S., Saito, M., Lim, J., Saigo, K., Sridharan, T. K., & Patel, N. A. 2012, *ApJ*, 754, 52
- Takakuwa, S., Saito, M., Lim, J., & Saigo, K. 2013, *ApJ*, 776, 51
- Takakuwa, S., Saito, M., Saigo, K., Matsumoto, T., Lim, J., Hanawa, T., & Ho, P. T. P. 2014, *ApJ*, in press
- Tobin, J. J., Hartmann, L., Chiang, H.-F., Wilner, D. J., Looney, L. W., Loinard, L., Calvet N., & D’Alessio, P. 2012, *Nature*, 492, 83
- Wu, P.-F., Takakuwa, S., & Lim, J. 2009, *ApJ*, 698, 184
- Yen, H.-W., Takakuwa, S., Ohashi, N., & Ho, P. T. P. 2013, *ApJ*, 772, 22
- Yen, H.-W., Takakuwa, S., & Ohashi, N., et al. 2014, *ApJ*, 793, 1

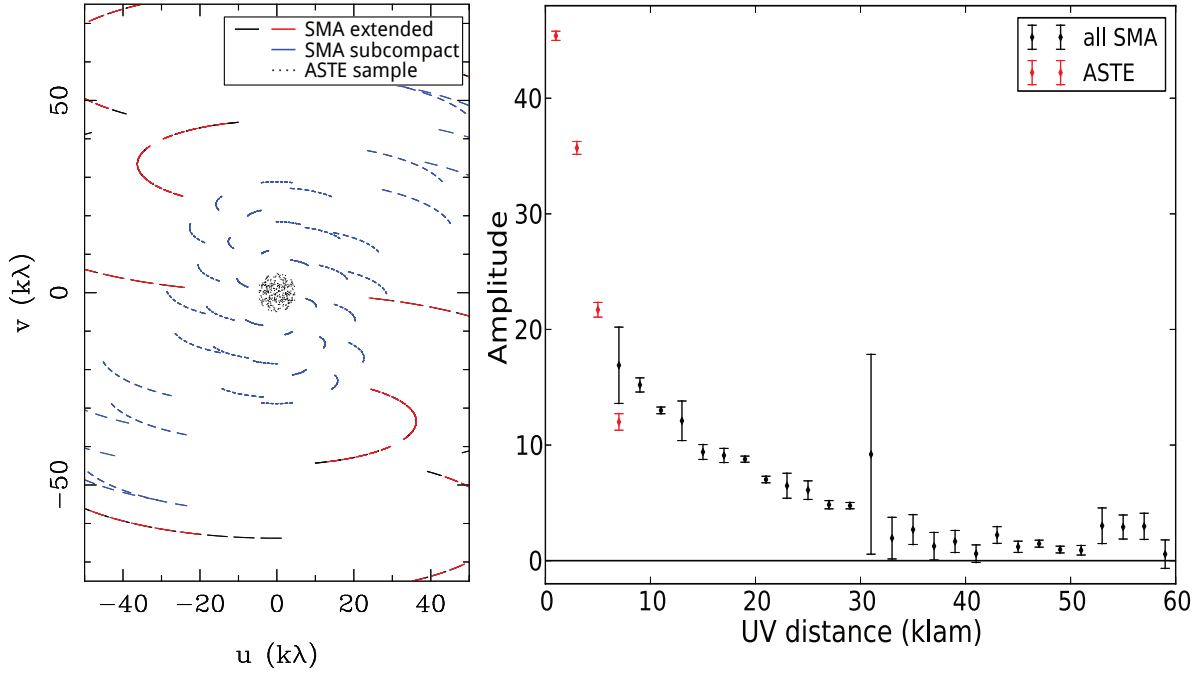


Fig. 1.— Plots of the  $uv$  coverages (*left*) and the  $uv$ -distances v.s. amplitudes of the SMA and ASTE datasets in the CS (7–6) emission (*right*). In the left panel, black and red lines represent the  $uv$  coverages taken with the SMA extended configuration at the two epochs, blue lines with the SMA subcompact configuration, and black dots the  $uv$  sample points adopted for the ASTE data. In the right panel, the black data points show the mean values and the standard deviations of the SMA visibility data and the red points those of the ASTE data at a  $2\text{ k}\lambda$  bin in the velocity range from  $V_{LSR} = 5.6\text{ km s}^{-1}$  to  $7.7\text{ km s}^{-1}$ .

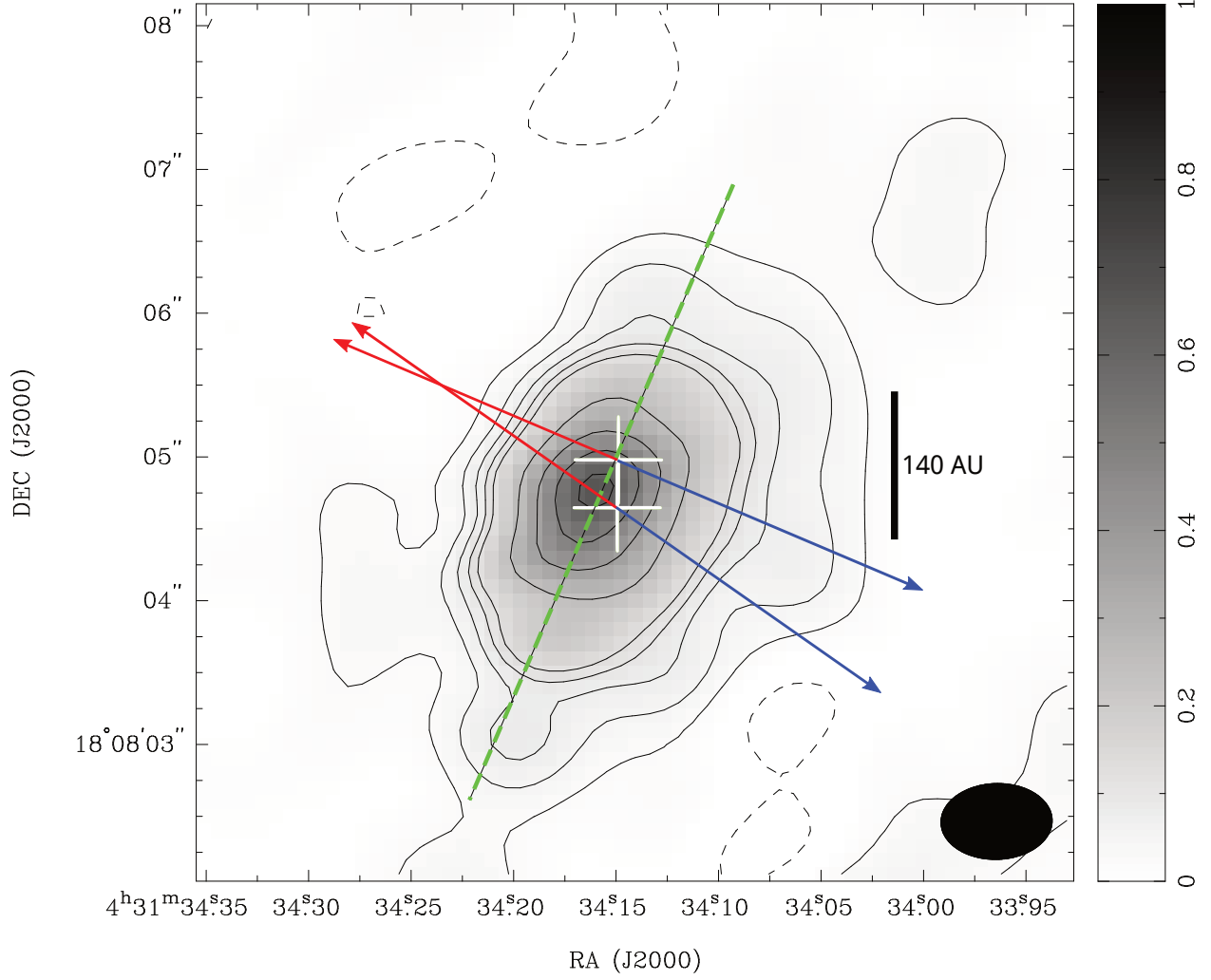


Fig. 2.— 343 GHz continuum image of L1551 IRS 5 observed with the SMA. Contour levels are from  $3\sigma$  in steps of  $3\sigma$  until  $15\sigma$ , and then in steps of  $15\sigma$  ( $1\sigma = 8.4 \text{ mJy beam}^{-1}$ ). The highest contour level is  $75\sigma$ . A filled ellipse at the bottom-right corner denotes the synthesized beam size ( $0''.77 \times 0''.53$ ; P.A. =  $-88^\circ$ ). Crosses show the positions of the protobinary in L1551 IRS 5 taken from Lim & Takakuwa (2006). A green dashed line shows the major axis of the 343 GHz continuum emission as measured from the 2-dimensional Gaussian fitting, and blue and red arrows show the direction of the blueshifted and redshifted jets driven by the protobinary.

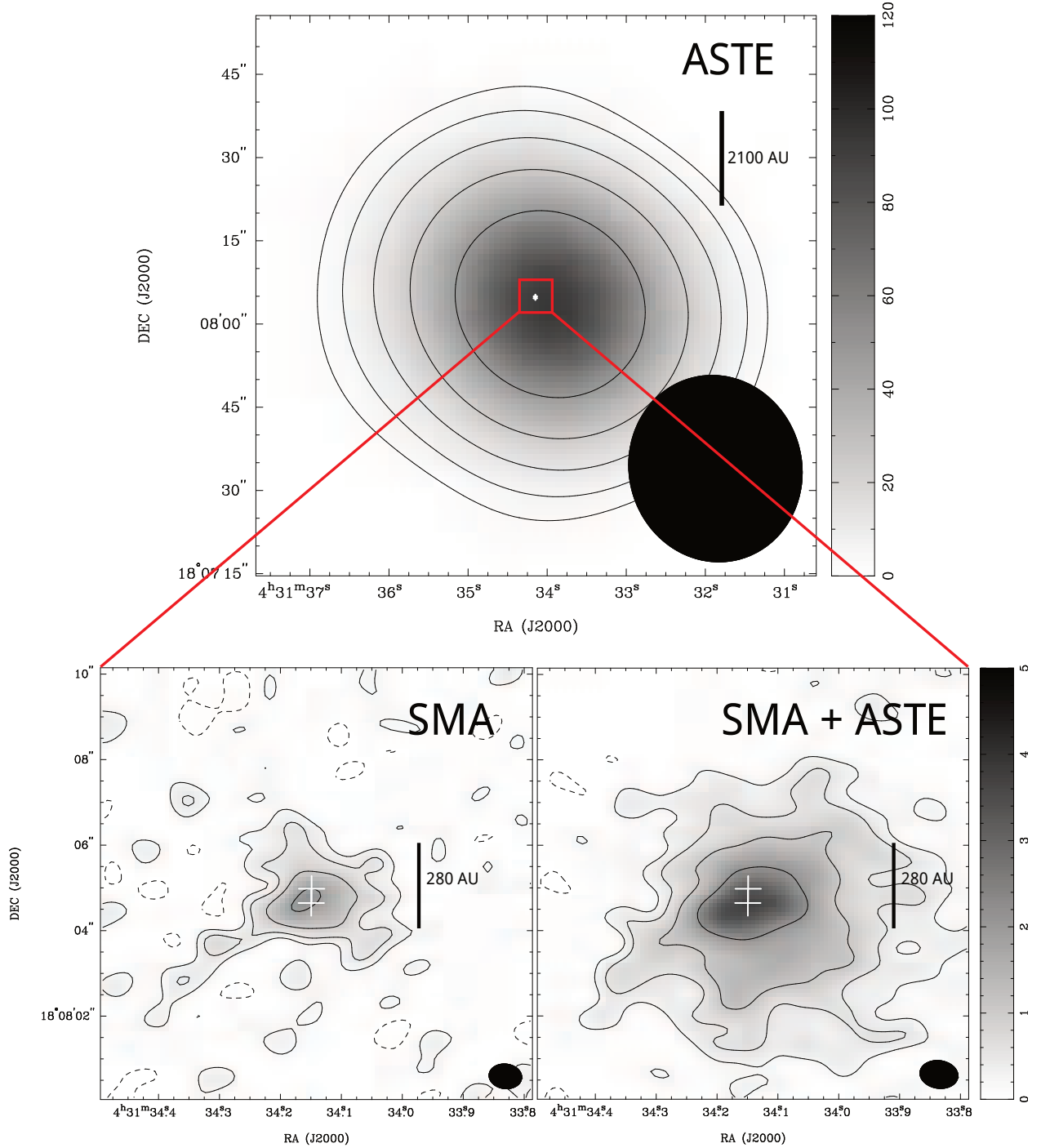


Fig. 3.— Comparison of the ASTE, SMA, and the combined SMA + ASTE moment 0 maps of the CS (7–6) emission in L1551 IRS 5. The integrated velocity range is  $V_{\text{LSR}} = 3.8 - 9.3 \text{ km s}^{-1}$ . Contour levels are  $2\sigma$ ,  $4\sigma$ ,  $8\sigma$ ,  $16\sigma$ , and  $32\sigma$  ( $1\sigma = 1.52$ ,  $0.122$ , and  $0.133 \text{ Jy beam}^{-1} \text{ km s}^{-1}$  in the ASTE, SMA, and the SMA+ASTE maps). Filled ellipses at the bottom-right corners of the images denote the synthesized beam sizes ( $22''$  for the ASTE image,  $0''.77 \times 0''.58$ , P.A. =  $83^\circ$  for the SMA image, and  $0''.90 \times 0''.65$ , P.A. =  $82^\circ$  for the SMA + ASTE image.) Crosses show the positions of the protobinary.



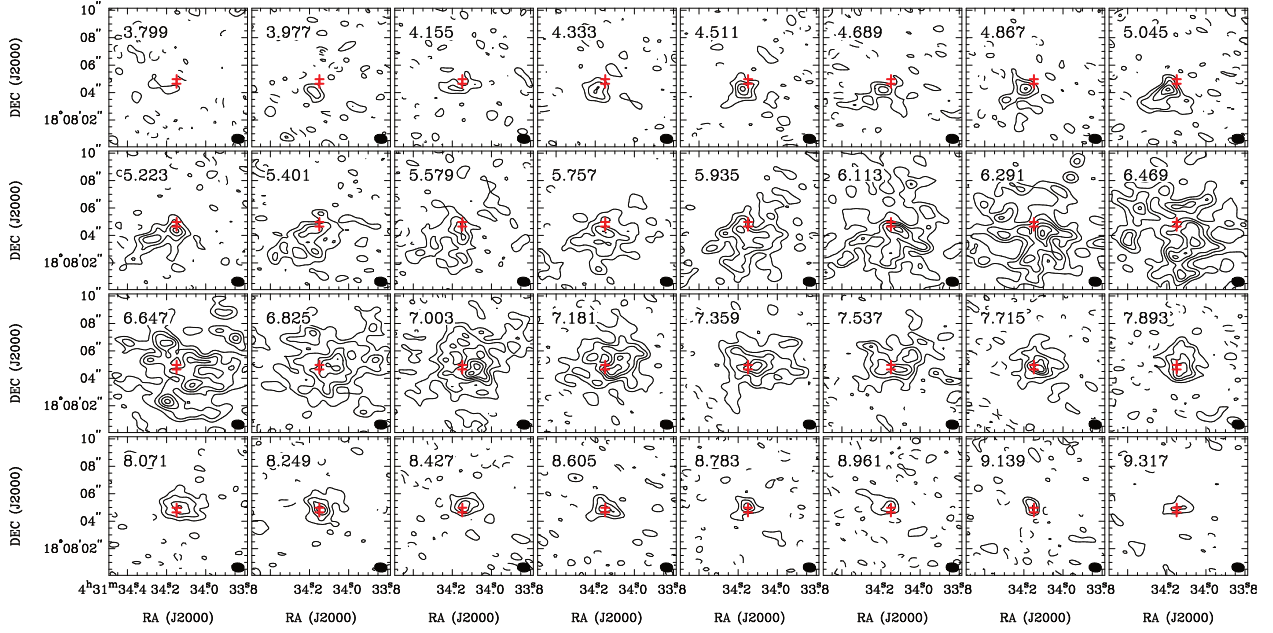


Fig. 4.— SMA + ASTE velocity channel maps of the CS (7–6) line in L1551 IRS 5. Contour levels are from  $2\sigma$  in steps of  $2\sigma$  ( $1\sigma = 0.130 \text{ Jy beam}^{-1}$ ). Crosses indicate the positions of the protobinary, and a filled ellipse at the bottom-right corner in each panel the synthesized beam ( $0''.90 \times 0''.65$ ; P.A. =  $82^\circ$ ). A number at the top-left corner in each panel denotes the LSR velocity.

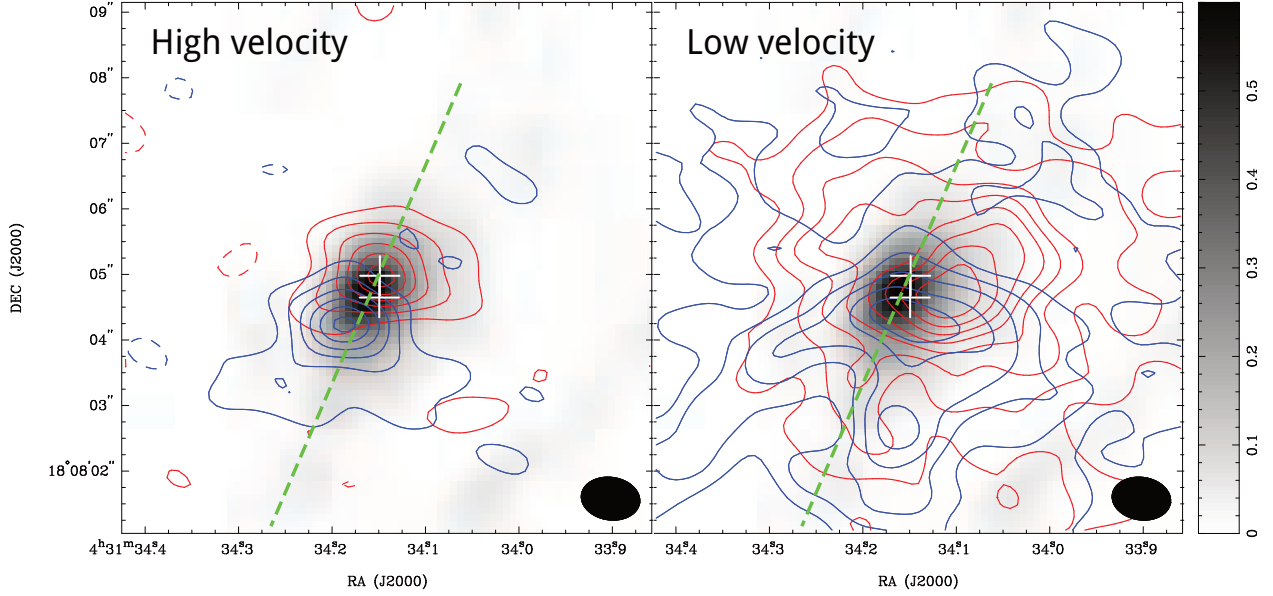


Fig. 5.— Distributions of the high- and low-velocity blueshifted (*blue contours*) and redshifted (*red*) CS (7–6) emission in L1551 IRS 5 obtained with the SMA and ASTE, superposed on the 343 GHz continuum image (*grey scale*). Contour levels are from  $3\sigma$  in steps of  $3\sigma$ . The  $1\sigma$  rms noise levels of the high-velocity blueshifted, redshifted, low-velocity blueshifted, and redshifted emission are 0.065, 0.077, 0.065, 0.057 Jy beam $^{-1}$  km s $^{-1}$ , respectively, and the integrated velocity ranges are 3.799 km s $^{-1}$  – 5.045 km s $^{-1}$ , 8.071 km s $^{-1}$  – 9.495 km s $^{-1}$ , 5.223 km s $^{-1}$  – 6.469 km s $^{-1}$ , and 6.647 km s $^{-1}$  – 7.893 km s $^{-1}$ , respectively. Crosses show the positions of the protobinary. A filled ellipse at the bottom-right corner in each panel denotes the synthesized beam ( $0''.90 \times 0''.65$ ; P.A. =  $82^\circ$ ). Dashed lines show the major axis of the 343 GHz continuum emission.

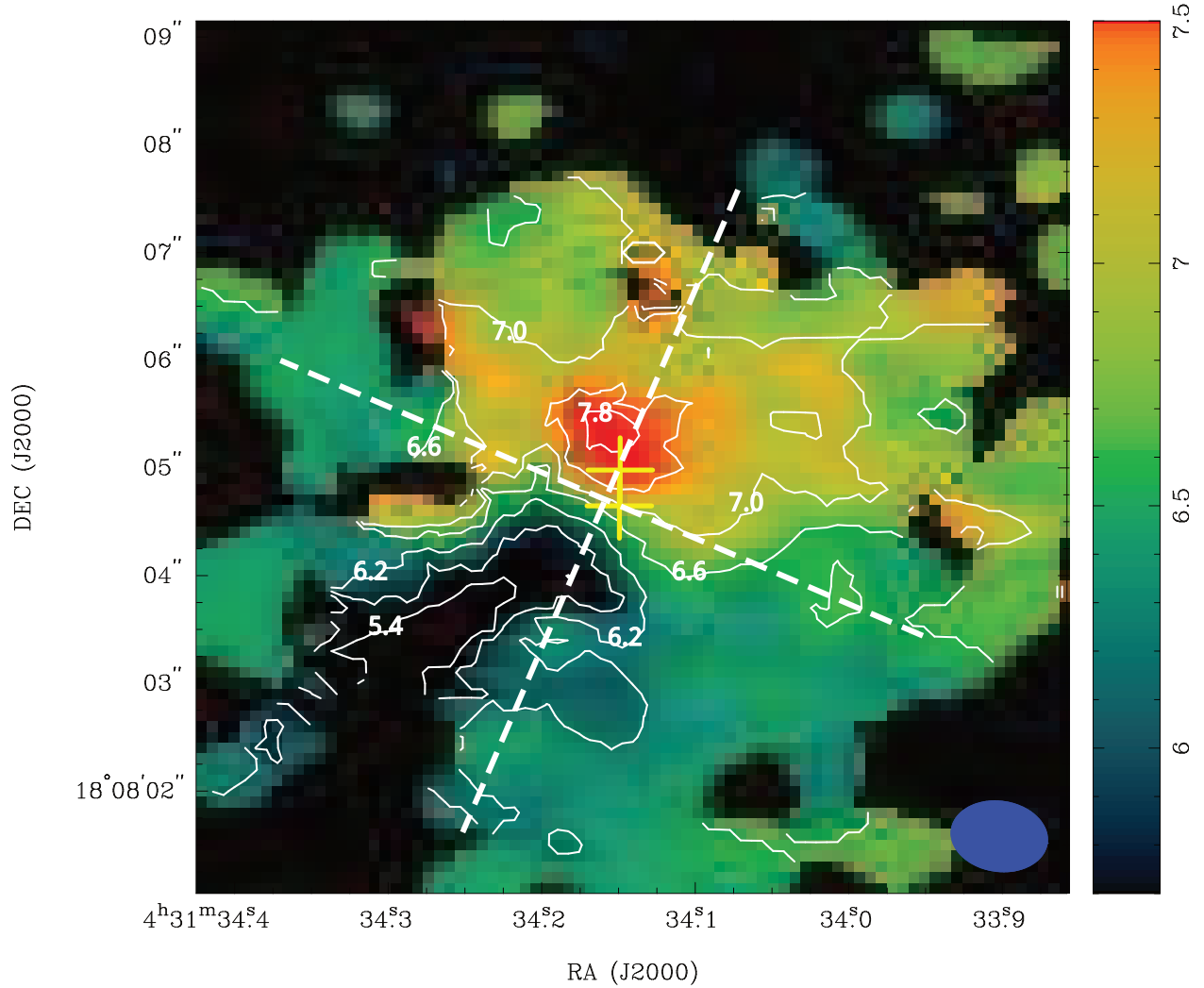


Fig. 6.— SMA + ASTE moment 1 map of the CS (7–6) emission in L1551 IRS 5. Yellow crosses show the positions of the protobinary, and white dashed lines the major and minor axes of the 343 GHz continuum emission. Contour levels are in steps of  $0.4 \text{ km s}^{-1}$ , and the bluest and reddest contour levels to the south-east and north-west of the protobinary are  $5.4 \text{ km s}^{-1}$  and  $7.8 \text{ km s}^{-1}$ , respectively. Some of the contours are also labeled with their values. A filled ellipse at the bottom-right corner denotes the synthesized beam size ( $0''.90 \times 0''.65$ ; P.A. =  $82^\circ$ ).

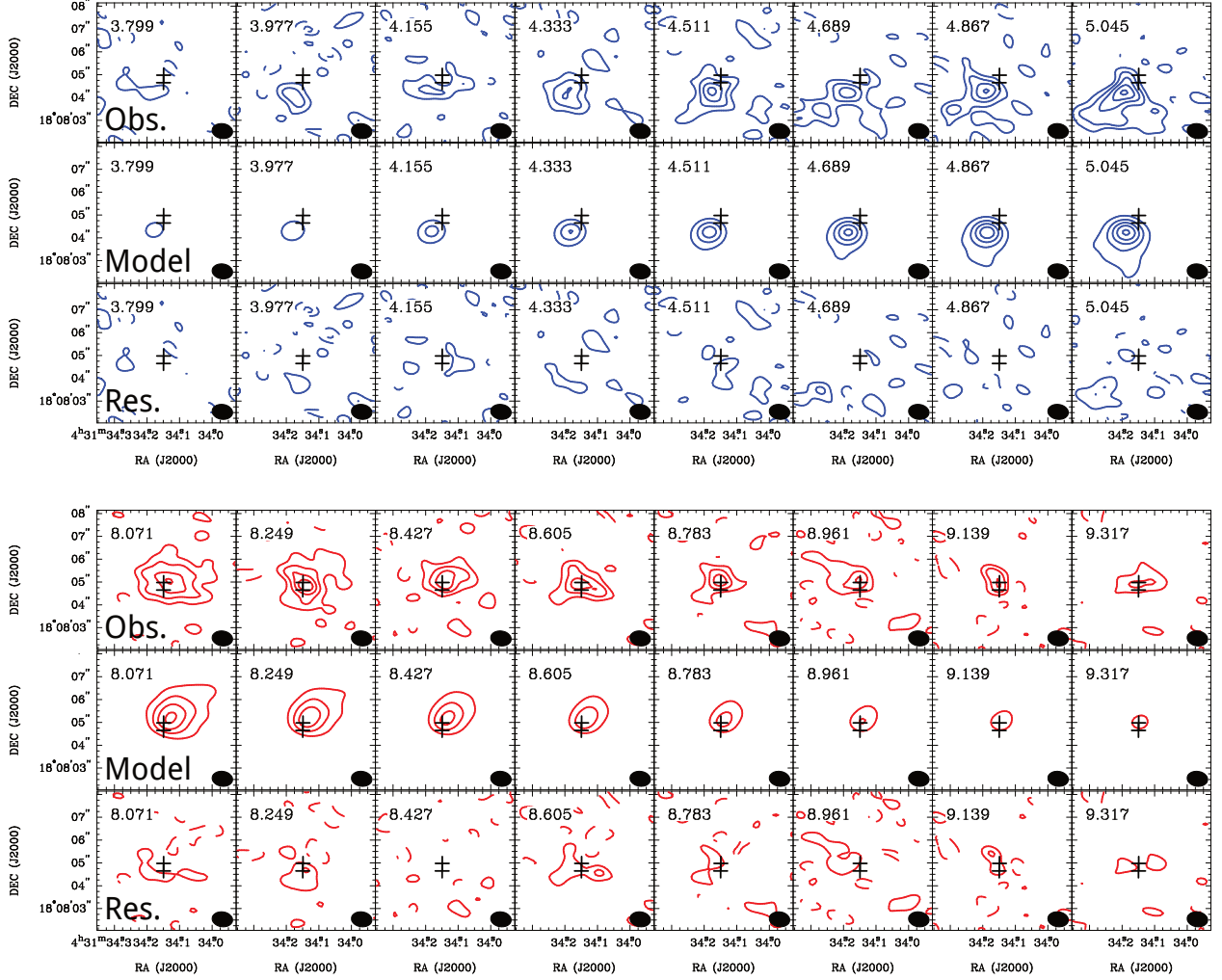


Fig. 7.— Best-fit results of the  $\chi^2$  model fitting of the geometrically-thin Keplerian disk to the SMA+ASTE CS (7-6) velocity channel maps in L1551 IRS 5 at the highly blueshifted (*blue contours*) and redshifted (*red*) velocities. Upper, middle, and lower panels show the observed, model, and the residual velocity channel maps, respectively, where the best-fit parameters are  $M_\star = 0.5 M_\odot$  and disk position angle  $\theta = -33^\circ$ . Contour levels are from  $2\sigma$  in steps of  $2\sigma$  ( $1\sigma = 0.130 \text{ Jy beam}^{-1}$ ). Crosses show the positions of the protobinary, and the filled ellipses at the bottom-right corners the SMA + ASTE synthesized beam ( $0''.90 \times 0''.65$ ;  $P.A. = -82^\circ$ ).

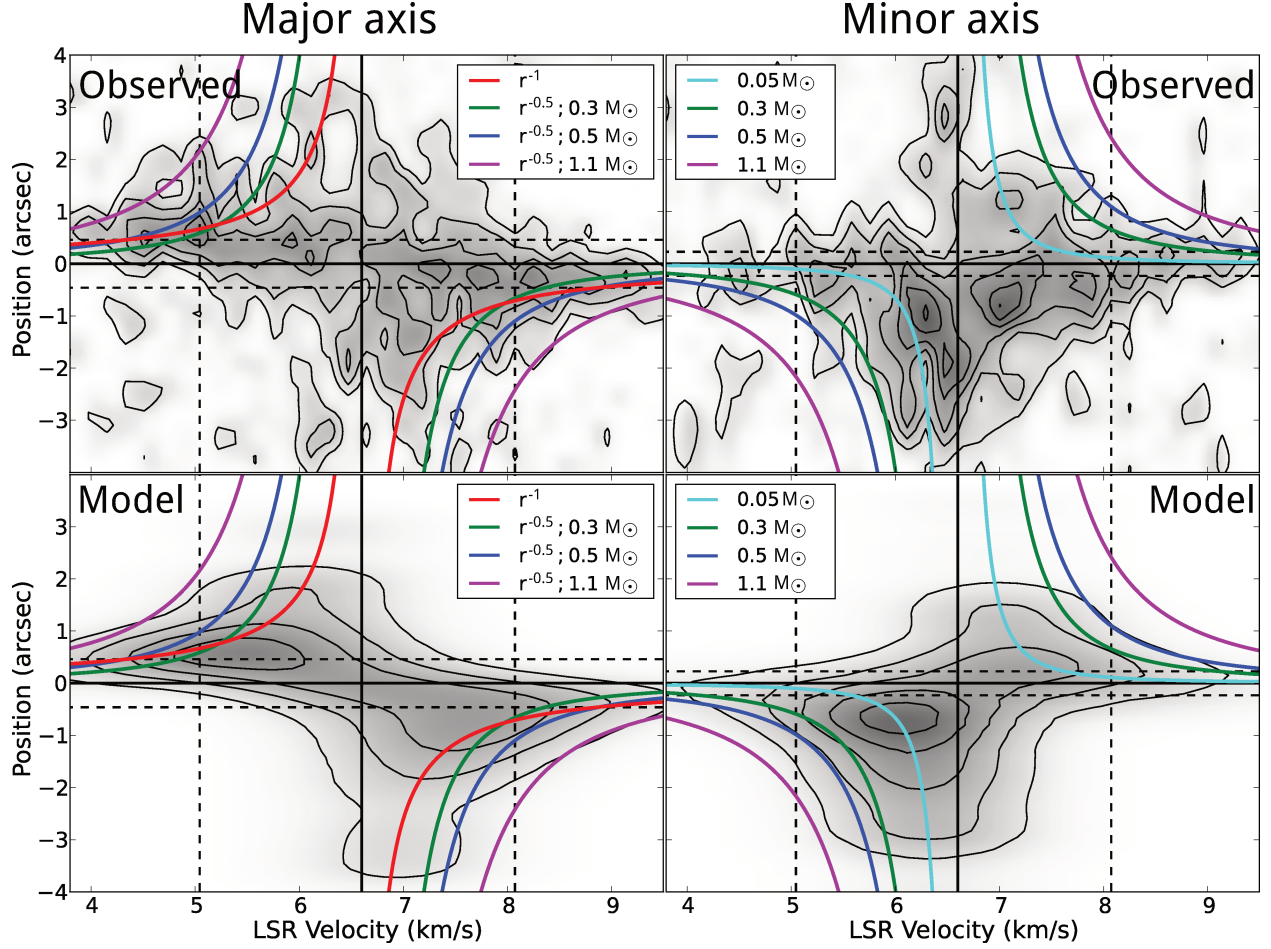


Fig. 8.— SMA+ASTE (*upper panels*) and model (*lower*) Position – Velocity (P-V) diagrams of the CS (7–6) emission in L1551 IRS 5 along the major (P.A. = 147°; *Left*) and minor axes (P.A. = 57°; *Right*) of the Keplerian circumbinary disk. Contour levels are from  $2\sigma$  in steps of  $2\sigma$  ( $1\sigma = 0.130 \text{ Jy beam}^{-1}$ ). Horizontal thick and dashed lines denote the centroid position of the 343 GHz continuum emission and the size of the the Keplerian disk (64 AU in halfwidth along the major axis and 32 AU along the minor axis), respectively. Vertical thick and dashed lines denote the systemic velocity ( $= 6.6 \text{ km s}^{-1}$ ) and the velocity borderline used in Figure 5 to separate the high-velocity and low-velocity components, respectively. In the left panels, the red curves show the rotation curve with a conserved angular momentum ( $j = 168 \text{ AU km s}^{-1}$ ); the green, blue, and purple curves show the Keplerian rotation curves with the central stellar masses of 0.3, 0.5, and  $1.1 M_{\odot}$ , respectively. In the right panels, cyan, green, blue, and purple curves show free-fall gas motions with the central stellar masses of 0.05, 0.3, 0.5, and  $1.1 M_{\odot}$ , respectively.

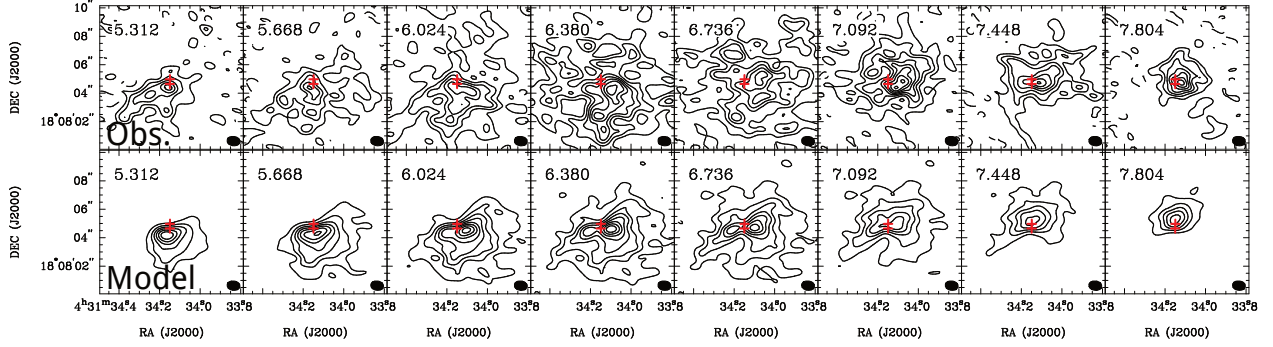


Fig. 9.— Comparison of the observed SMA+ASTE velocity channel maps of the CS line (*upper row*) to the velocity channel maps of the geometrically-thin infalling and rotating envelope model (*lower row*) at the lower velocities ( $-1.377 \text{ km s}^{-1} \sim 0.937 \text{ km s}^{-1}$  from the systemic velocity). Contour levels are from  $2\sigma$  in steps of  $2\sigma$  ( $1\sigma = 0.092 \text{ Jy beam}^{-1}$ ). Details of the model are described in Section 4.2. Crosses show the position of the protobinary, and filled ellipses at the bottom-right corners indicate the SMA + ASTE synthesized beam ( $0''.90 \times 0''.65$ ; P.A. =  $-82^\circ$ ).

Table 1. Parameters for the SMA Observations of L1551 IRS 5

Parameter	Value	
	SMA extended	SMA subcompact
Observation Date	2012 Dec 23, 2013 Jan 4	2009 Sep 21
Number of Antennas	7	7
Field Center	(04 <sup>h</sup> 31 <sup>m</sup> 34 <sup>s</sup> .14, 18°08′05″.1)	
Primary Beam HPBW	~36″	
Synthesized Beam HPBW (Continuum, SMA)	0′.77 × 0′.53 (P.A. = -88°)	
Synthesized Beam HPBW (CS line, SMA+ASTE)	0′.90 × 0′.65 (P.A. = 82°)	
Baseline Coverage	20.7 – 218.0 (m)	6.7 – 67.3 (m)
Frequency Coverage	328.9 – 332.9 GHz (LSB)	342.8 – 344.8 GHz (LSB)
	340.9 – 344.9 GHz (USB)	352.8 – 354.8 GHz (USB)
Conversion Factor (CS line, SMA+ASTE)	1 (Jy beam <sup>-1</sup> ) = 17.8 (K)	
Frequency Resolution	203 kHz ~0.178 km s <sup>-1</sup>	
Flux Calibrator	Neptune	Mars
Gain Calibrator	0423-013, 0530+135	0423-013, 3c120
Flux (0423-013)	1.82 Jy	3.65 Jy
Flux (0530+135)	0.30 Jy	
Flux (3c120)		0.86 Jy
System Temperature (DSB)	~350 – 1250 K	~180 – 330 K
rms noise level (Continuum, SMA)	8.4 mJy beam <sup>-1</sup>	
rms noise level (CS Line, SMA+ASTE)	0.130 Jy beam <sup>-1</sup>	

Table 2. Prototellar Sources with Keplerian Disks

Source	$L_{bol}$ ( $L_{\odot}$ )	$T_{bol}$ ( $K$ )	$R_{kep}^a$ (AU)	$M_{\star}^b$ ( $M_{\odot}$ )	$M_{disk}^c$ ( $M_{\odot}$ )	$M_{env}^d$ ( $M_{\odot}$ )	$\frac{M_{\star}}{M_{\star}+M_{disk}+M_{env}}$ (%)	References <sup>e</sup>
Class 0 sources								
VLA1623A	1.1	10	180	0.22	...	0.8	<22	1,2
L1527 IRS	1.97	44	50–90	0.19–0.3	0.007	0.9	17	3,4,5
Class I sources								
L1551 NE	4.2	91	300	0.8	0.026	0.39	65	2,6,7
L1551 IRS 5	22.1	94	64	0.5	0.070	1.01	32	This work,3,6
TMC1	0.9	101	100	0.54	0.005–0.024	0.14	78	3,8
TMC1A	2.7	118	100	1.1	0.025–0.06	0.12	88	3,8,9
L1489-IRS	3.7	238	200	1.8	0.007–0.02	0.11	95	9,10,11
L1536	0.4	270	80	0.4	0.007–0.024	0.05	86	3,8,12
Elias 29	14.1	299	200	2.5	$\lesssim 0.007$	0.025	$\gtrsim 99$	3,13
IRS 43	6.0	310	140	1.0	0.0081	0.026	97	11
IRS 63	1.0	327	100	0.37	0.055	0.022	83	3,13

**Notes.**

<sup>a</sup>Outer radius of the Keplerian disk.

<sup>b</sup>Central protostellar mass.

<sup>c</sup>Mass of the Keplerian disk.

<sup>d</sup>Mass of the protostellar envelope within the radii of  $\sim 10''$ – $15''$ .

<sup>e</sup>References: (1) Murillo et al. 2013; (2) Froebrich 2005; (3) Kristensen et al. 2012;

(4) Tobin et al. 2012; (5) Ohashi et al. 2014; (6) Moriarty-Schieven et al. 2006;

(7) Takakuwa et al. 2012; (8) Harsono et al. 2014; (9) Yen et al. 2013; (10) Brinch et al. 2007;

(11) Jørgensen et al. 2009; (12) Eisner 2012; (13) Lommen et al. 2008.